Weierstraß-Institut
für Angewandte Analysis und Stochastik

Leibniz-Institut im Forschungsverbund Berlin e. V.

Preprint ISSN 2198-5855

Optimal control of conveyor-mode spin-qubit shuttling in a Si/SiGe quantum bus in the presence of charged defects

Lasse Ermoneit[1], Burkhard Schmidt[1], Thomas Koprucki[1], Jürgen Fuhrmann[1], Tobias Breiten[2], Arnau Sala[3], Nils Ciroth[3], Ran Xue[3], Lars R. Schreiber[3,4], Markus Kantner[1]

submitted: December 22, 2023

[1] Weierstrass Institute
Mohrenstr. 39,
10117 Berlin, Germany
E-Mail: lasse.ermoneit@wias-berlin.de
burkhard.schmidt@wias-berlin.de
thomas.koprucki@wias-berlin.de
juergen.fuhrmann@wias-berlin.de
markus.kantner@wias-berlin.de

[2] Institute of Mathematics
Technical University Berlin
Straße des 17. Juni 136
10623 Berlin, Germany
E-Mail: tobias.breiten@tu-berlin.de

[3] JARA Institute for Quantum Information,
Forschungszentrum Jülich GmbH and
RWTH Aachen University
52074 Aachen, Germany
E-Mail: a.sala.cadellans@fz-juelich.de
ran.xue@rwth-aachen.de
nils.ciroth@physik.rwth-aachen.de
lars.schreiber@physik.rwth-aachen.de

[4] ARQUE Systems GmbH
Campus Boulevard 30
52074 Aachen, Germany

No. 3082
Berlin 2023

2020 *Mathematics Subject Classification.* 35Q41, 35Q81, 78A30, 78M12, 81V65, 93C95.

Key words and phrases. Spin-qubits, quantum computers, quantum dots, semiconductor device simulation, quantum optimal control, Schrödinger wave packet propagation, Landau–Zener transition.

This work was funded by the German Research Foundation (Deutsche Forschungsgemeinschaft, DFG) under Germany's Excellence Strategy – EXC2046: MATH+ and under Germany's Excellence Strategy – Cluster of Excellence Matter and Light for Quantum Computing ML4Q (EXC-2004/1, project ID 390534769).

Edited by
Weierstraß-Institut für Angewandte Analysis und Stochastik (WIAS)
Leibniz-Institut im Forschungsverbund Berlin e. V.
Mohrenstraße 39
10117 Berlin
Germany

Fax: +49 30 20372-303
E-Mail: preprint@wias-berlin.de
World Wide Web: http://www.wias-berlin.de/

Optimal control of conveyor-mode spin-qubit shuttling in a Si/SiGe quantum bus in the presence of charged defects

Lasse Ermoneit, Burkhard Schmidt, Thomas Koprucki, Jürgen Fuhrmann, Tobias Breiten, Arnau Sala, Nils Ciroth, Ran Xue, Lars R. Schreiber, Markus Kantner

Abstract

Spin-qubit shuttles are novel functional elements in modular architectures of semiconductor quantum processors, that have the capability of solving the scalability problem. Such coherent quantum links serve to interconnect different processor units and enable the transfer of quantum information over longer distances across the chip by physical transport of electrons. The shuttling fidelity is limited by hardly avoidable material defects and fabrication imperfections, which can cause spin dephasing. In this paper, we present a numerical simulation framework for conveyor-mode spin-qubit shuttling in Si/SiGe and investigate the impact of charged defects in the channel on the orbital state dynamics of the transported electron. Quantum optimal control theory is employed to engineer control pulses that enable nearly deterministic passage of the electron through the channel by minimizing the accumulated energy uncertainty. The resulting control pulses facilitate quasi-adiabatic driving of the electron by circumventing critical regions in the channel without reducing the shuttling speed. Moreover, we demonstrate that trailing electrons subject to the same control pulse at a defect-free segment of the channel are not disturbed by the control. The theoretical results serve as a guideline for fine-tuning the controls in spin-qubit shuttling experiments.

1 Introduction

Spin-qubits in electrostatically defined semiconductor quantum dots (QDs) in Si/SiGe heterostructures are one of the major candidates for the realization of scalable universal quantum computers [1–4]. By using isotopically purified nuclear spin-free ^{28}Si in the quantum well (QW), the coherence time can be extended up to the millisecond range by suppressing the hyperfine interaction with the background nuclear spins [5–7]. In recent years, one- and two-qubit gates have been demonstrated with high fidelity sufficient for fault-tolerant quantum computing [8–13]. Due to its compatibility with industrial fabrication processes and the tiny footprint of semiconductor QDs, the technology has excellent prospects for scalability to very large qubit registers [3, 14]. As a landmark step on this route, Intel unveiled its first 12-qubit silicon quantum processor *Tunnel Falls* in June 2023, which was manufactured using an only slightly modified CMOS processing line [15].

A major challenge in the realization of large qubit arrays is the wiring of a large number of lithographically defined QDs in a small space. Each individual QD requires several leads for confinement, signaling and readout, which potentially have to be stacked in multiple layers [14, 16]. Next to geometric limitations, also heating effects and unintended crosstalk between qubits can become a significant problem. A potential remedy to this issue is a modular architecture in which small and medium-sized qubit arrays are interlinked by a quantum bus for coherent transmission of quantum information [14, 17]. In such a quantum bus, an electron is shuttled adiabatically through a channel in order to transfer the quantum information encoded in the spin between different functional units of the processor. In addition to solving

DOI 10.20347/WIAS.PREPRINT.3082 Berlin 2023

the aforementioned *fanout problem* (*i.e.*, the wiring bottleneck), this concept also provides sufficient space for on-chip integration of classical control electronics [14].

Two different modes of electron shuttling have been investigated so far: In the *bucket-brigade mode* [18–23], the electron is transported through an array of tunnel-coupled QDs via a sequence of adiabatic Landau–Zener transitions. In this process, the tunnel barriers between the QDs are sequentially controlled by voltage pulses so that the electron wave packet is propagated adiabatically along the array. The alternative to this is *conveyor-mode shuttling* [21, 24–26], in which a moving QD potential is generated that conveys the electron adiabatically along the channel. In realistic devices with potential disorder and material defects, the bucket brigade mode requires extensive tuning of the individual voltage pulses, which severely limits the scalability of the approach. Conveyor-mode shuttling, on the other hand, is more robust to fabrication imperfections and permits the implementation of scalable concepts in which the shuttling distance can be made independent of the number of control signals [21]. Such qubit shuttles can, on the one hand, interlink different functional modules such as memory or processor units [27], but on the other hand also allow for execution of quantum gate operations directly in the shuttle [28]. Recent concepts for small-scale quantum processors therefore envisage networks of qubit shuttles, which comprise dedicated manipulation zones for the implementation of quantum gate operations [28, 29].

For the realization of such scalable solid-state architectures, the impact and mitigation of unavoidable material imperfections has to be considered [30]. In the Si/SiGe platform these are typically charge noise and disorder due to charged defects [8, 31, 32], alloy disorder of the SiGe barrier and interface segregation [33], unintentional strain [34] and line-edge roughness of electrostatic gates [35]. Concerning the Si-QuBus, the effect of electrostatic disorder from remote charge defects at the interface of the silicon and the amorphous dielectric [21, 25] and strain induced by metallic gates [36] have been explored.

In the present work, we theoretically investigate the effects of highly dilute charge defects within the epitaxially grown Si/SiGe heterostructure as they occur in real devices and analyze the feasibility of control pulse engineering to circumvent critical areas. Specifically, we consider one negatively charged impurity very close to the active region of the *Si-QuBus* shuttling device [21]. We will briefly outline the device concept in Sec. 2. In Sec. 3, we present the theoretical model for numerical simulation of electron shuttling. The primary focus in our simulations is on orbital excitations caused by interaction of the electron with charged impurities. The major contribution of this work is the application of quantum optimal control theory to engineer optimized control pulses for bypassing a charged defect, see Sec. 4. The objective is to steer the electron around the defect on a deterministic trajectory, which is characterized by a minimum accumulated energy uncertainty. Our approach self-consistently considers the control-induced change of the potential landscape and the corresponding evolution of the electron's energy uncertainty and deduces an optimal control pulse following a variational principle. The results are discussed in Sec. 5.

2 Device Concept

We consider the spin-qubit shuttling device *Si-QuBus*, which is depicted in Fig. 1, that was described in detail by Langrock *et al.* [21]. The device contains an undoped SiGe/Si/SiGe QW in which a two-dimensional electron gas can be accumulated by the top-gates. On the top surface, the Si-QuBus features a periodic pattern of so-called *clavier gates*, see Fig. 1, where every fourth clavier gate is electrically connected to all the others in the chain. By applying phase-shifted sinusoidal voltages at

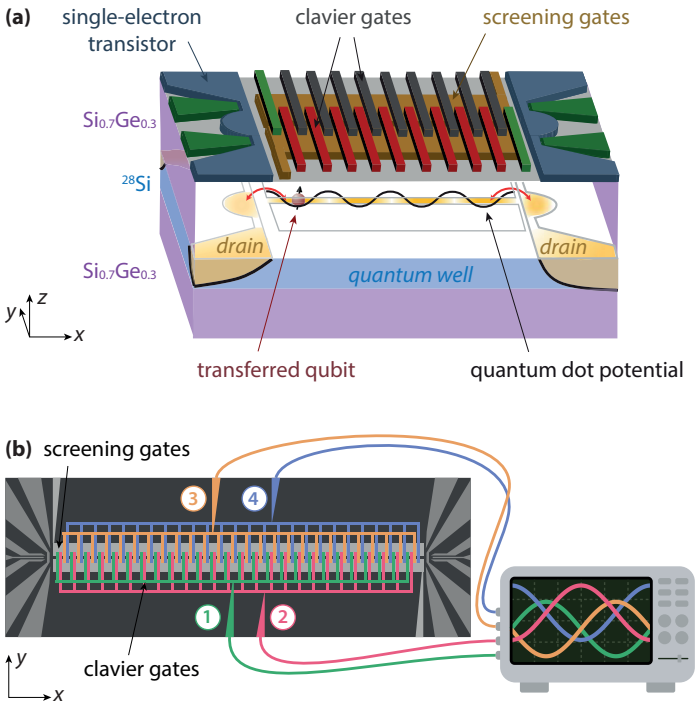

Fig. 1. (a) Schematic illustration of the Si-QuBus device. The clavier gate electrodes on the top surface generate a moving array of QD potentials that allow to transport the electron spin-qubit in a conveyor-mode along the channel. **(b)** Top view on the Si-QuBus with the four different clavier gate sets highlighted in color. Conveyor-mode shuttling requires only four different control pulses, independent of the channel length, which is an important factor for the scalability of the approach. The two screening gates on the left and the right hand side of the channel are employed to bypass a charged defect in the channel by optimally engineered voltage pulses in Sec. 4. The pictures are adapted from [21, Fig. 2 and 5] used under CC-BY.

the clavier gates, a linear array of QD potentials is formed in the QW, where the step-like epitaxial QW confinement potential (in the z-direction) is superimposed with the potential generated by the gate electrodes on the top surface of the structure. By continuously driving the phase of the clavier gate voltages, the QDs can be propagated along the channel. As the device requires only four voltage signals to drive the whole set of clavier gates—regardless of the length of the channel—this conveyor-mode technique for electron shuttling can be scaled up to large architectures [21]. Underneath the clavier gates, the device contains two long screening gates, the gap between which defines the one-dimensional channel for the shuttling of the electron. The voltage applied to the two screening gates serve for tuning of the lateral confinement. In addition, the trajectory of the lateral coordinate of the shuttled electron can be controlled by proper pulsing of the screening gates. In Sec. 4, we investigate the implementation of dynamical displacement of the electron using the screening gates in order to achieve quasi-adiabatic passage of a charged defect in the channel.

3 Simulation of Electron Shuttling

In this section, we describe the mathematical model and the numerical simulation framework to simulate coherent single-electron shuttling in the Si-QuBus. We focus on the dynamics of orbital excitations triggered by Landau–Zener transitions [37] at charged impurities and investigate optimal control strategies to achieve quasi-adiabatic driving in the presence of charged defects. Spin and valley states as well as the respective interactions are neglected in this work. Moreover, the current model is limited to the coherent wave packet evolution and disregards the effects of noise and dissipation.

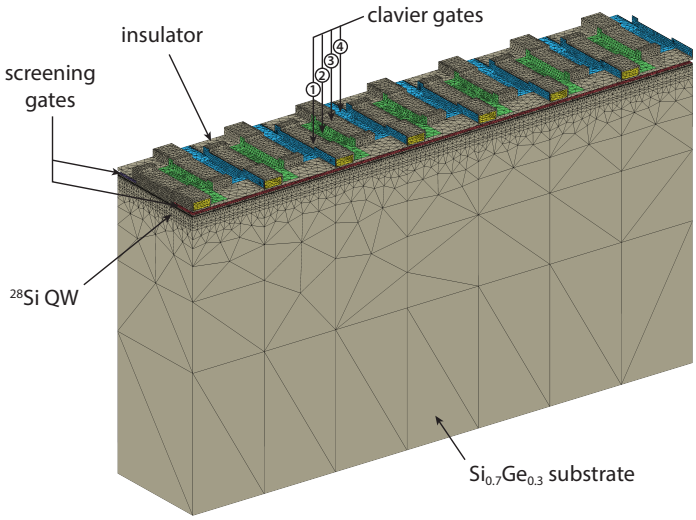

Fig. 2. Coarse grained Delaunay mesh of the device with seven unit cells. The refined computational mesh for the solution of Poisson's problem (1) includes about 20 million nodes and was generated using TetGen [38].

3.1 Electric Potential

The gate electrodes form an electric potential landscape that generates an array of QDs in the QW. Suitable pulsing allows to propagate the QDs along the channel and thus enables conveyor-mode shuttling. As the device is operated at deep cryogenic temperature (50 mK), there exist no thermally activated electrons in the conduction band and space charge regions can be safely neglected. In this case, the electric potential $\Phi(\mathbf{r}, t)$ obeys the homogeneous Poisson equation

$$-\nabla \cdot (\varepsilon(\mathbf{r}) \nabla \Phi(\mathbf{r}, t)) = 0, \tag{1a}$$

where $\varepsilon(\mathbf{r}) = \varepsilon_0 \varepsilon_r(\mathbf{r})$ is the static dielectric permittivity of the semiconductor or insulator, respectively. The boundary conditions

$$\begin{aligned} \Phi(\mathbf{r}, t)|_{\Gamma_k} &= U_k^{\text{tot}}(t), \\ \mathbf{n} \cdot \nabla \Phi(\mathbf{r}, t)|_{\Gamma_N} &= 0, \\ \Phi(\mathbf{r}, t)|_{\Gamma_{\text{period}}} &= \Phi(\mathbf{r} + \mathbf{e}_x L_x, t) \end{aligned} \tag{1b}$$

describe the time-dependent applied voltages $U_k^{\text{tot}}(t)$ at the electrode interfaces Γ_k $(k = 1 \ldots 6)$ (Dirichlet boundary conditions) and artificial boundary conditions on the remaining surface Γ_N (homogeneous Neumann conditions), see Fig. 2. The device contains numerous periodically repeated unit cells with four clavier gates each. In the following, we consider a single unit cell of length L_x and assume periodic boundary conditions on the front and rear (y, z)-plane. The applied voltage

$$U_k^{\text{tot}}(t) = U_k(t) + u_k(t) \qquad k = 1, \ldots, 6 \tag{2}$$

is decomposed into a nominal pulse sequence $U_k(t)$ and a correction pulse $u_k(t)$. The correction pulse $u_k(t)$ will be adjusted such that charged defects can be adiabatically circumvented and will be computed in Sec. 4. The nominal pulse sequence at the clavier gates reads

$$U_{k=1,\ldots,4}(t) = U_k^{\text{DC}} + U_k^{\text{AC}} \sin\left(\frac{k\pi}{2} + 2\pi f_s t + \varphi_0\right). \tag{3}$$

Neighboring electrodes therefore have a phase difference of $\pi/2$, so that a QD potential can be formed [21]. The confinement depth of the QDs is governed by the amplitudes U_k^{AC} and the static offset U_k^{DC}.

voltage	description	weak confinement	strong confinement
$U^{\mathrm{DC}}_{k=1,3}$	lower clavier gates DC voltage	0.55 V	0.55 V
$U^{\mathrm{DC}}_{k=2,4}$	upper clavier gates DC voltage	0.70 V	0.70 V
$U^{\mathsf{AC}}_{k=1\ldots4}$	clavier gate amplitude	0.10 V	0.25 V
$U^{\mathrm{DC}}_{k=5,6}$	screening gates voltage	0 V	0 V

Tab. 1. Parameters of the nominal voltage sequence (3) for the two different confinement modes.

The shuttling phase

$$\varphi\left(t\right) = 2\pi f_s t \tag{4}$$

is a linear function of time, where f_s is the shuttling frequency. The shuttling frequency in turn is related to the shuttling velocity $v_s = L_x f_s$, which should be chosen around $v_s = 10\,\mathrm{m/s}$, see [21] for a discussion. The phase can be shifted by an arbitrary offset, which is chosen as $\varphi_0 = 0.75\,\pi$ throughout. The screening gates are nominally operated with a constant voltage: $U_{k=5,6}\left(t\right) = U_k^{\mathrm{DC}}$. In the following, we will consider a *weak confinement mode* and a *strong confinement mode*, which differ in the clavier gate amplitude. The respective voltage parameters are listed in Tab. 1.

The decomposition of the applied voltages (2) corresponds to a decomposition of the total electric potential

$$\Phi\left(\mathbf{r},t\right) = \Phi_0\left(\mathbf{r},t\right) + \Phi_{\mathsf{ctrl}}\left(\mathbf{r},t\right) \tag{5}$$

into a nominal part $\Phi_0\left(\mathbf{r},t\right)$ and a control part $\Phi_{\mathsf{ctrl}}\left(\mathbf{r},t\right)$. Due to the linearity of Poisson's problem (1), both parts can be further decomposed into the contributions from separate electrodes

$$\Phi_0\left(\mathbf{r},t\right) = \sum_{k=1}^{6} U_k\left(t\right)\phi_k\left(\mathbf{r}\right), \tag{6a}$$

$$\Phi_{\mathsf{ctrl}}\left(\mathbf{r},t\right) = \sum_{k=1}^{6} u_k\left(t\right)\phi_k\left(\mathbf{r}\right). \tag{6b}$$

Here, the $\phi_k\left(\mathbf{r}\right)$ are non-dimensionalized shape functions of the electrodes that obey the stationary Poisson problem

$$\begin{aligned} -\nabla\cdot\left(\varepsilon\left(\mathbf{r}\right)\nabla\phi_k\left(\mathbf{r}\right)\right) &= 0,\\ \phi_k\left(\mathbf{r}\right)|_{\Gamma_l} &= \delta_{k,l},\\ \mathbf{n}\cdot\nabla\phi_k\left(\mathbf{r}\right)|_{\Gamma_N} &= 0,\\ \phi_k\left(\mathbf{r}\right)|_{\Gamma_{\mathsf{period}}} &= \phi_k\left(\mathbf{r}+\mathbf{e}_x L_x\right), \end{aligned} \tag{7}$$

where $\delta_{k,l}$ is the Kronecker symbol. The numerically computed shape functions are shown in Fig. 3.

For the numerical simulation it is sufficient to solve the stationary Poisson problem (7) once for each of the six electrodes for a given geometry. We employ a finite volume method implemented in the Julia package *VoronoiFVM.jl* [39] to discretize Eq. (7) and solve the resulting system of linear equations via conjugate gradient iteration. A complete list of material parameters employed in the simulation is given in Tab. 3.

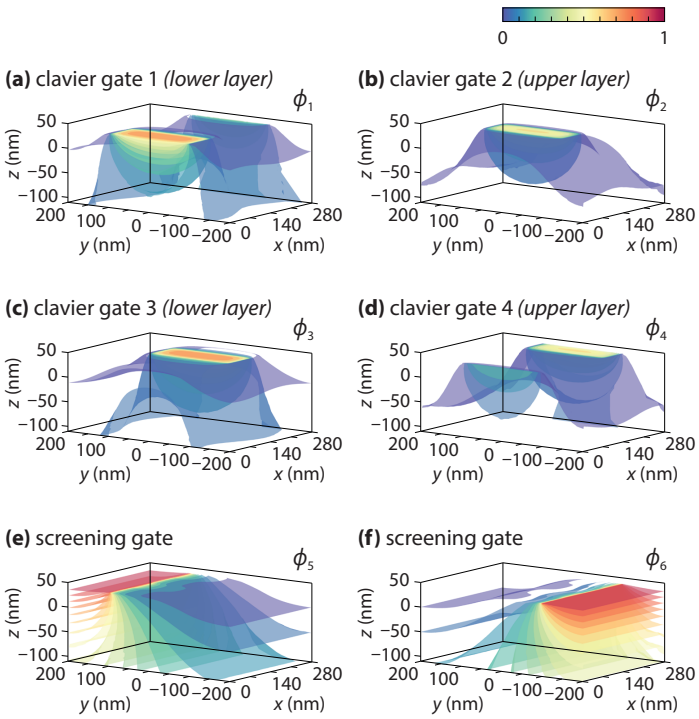

Fig. 3. Normalized gate electrode shape functions $\phi_k(\mathbf{r})$ solving the stationary Poisson problem (7). **(a)–(d)** clavier gates and **(e)–(f)** screening gates.

3.2 Time-Dependent Schrödinger Equation

Propagation of the electron wave packet $\Psi(\mathbf{r}, t)$ is described by the time-dependent Schrödinger equation (TDSE)

$$i\hbar \frac{\partial}{\partial t} \Psi(\mathbf{r}, t) = H(\mathbf{r}, t)\, \Psi(\mathbf{r}, t)\,. \tag{8}$$

The Hamiltonian is explicitly time-dependent as it includes the time-dependent electric potential $\Phi(\mathbf{r}, t)$. Following the decomposition (5) of the electric potential into a nominal and a control-related part, also the Hamiltonian is separated into two parts:

$$H(\mathbf{r}, t) = H_0(\mathbf{r}, t) + H_{\mathrm{ctrl}}(\mathbf{r}, t)\,. \tag{9}$$

The reference Hamiltonian reads

$$\begin{aligned} H_0(\mathbf{r}, t) = -\frac{\hbar^2}{2} \nabla \cdot \left(\frac{1}{m_e^*(\mathbf{r})} \nabla \right) - e_0 \Phi_0(\mathbf{r}, t) \\ + V_{\mathrm{QW}}(\mathbf{r}) + V_{\mathrm{defect}}(\mathbf{r})\,, \end{aligned} \tag{10}$$

where the first term describes the kinetic energy of a Si conduction band electron in a single-band, effective mass approximation, where $m_e^*(\mathbf{r})$ the effective mass. The second term is the potential energy due to the nominal electric potential $\Phi_0(\mathbf{r}, t)$ determined by the voltage sequence (3), where e_0 is the elementary charge. Furthermore, the reference Hamiltonian includes the step-like QW confinement potential $V_{\mathrm{QW}}(\mathbf{r})$ and the potential landscape of charged defects $V_{\mathrm{defect}}(\mathbf{r})$. Throughout this work, we consider a negatively charged point defect near the center of the QW as a guiding example, see Appendix B. The material parameters are listed in Tab. 3. The control Hamiltonian describes an additive correction to the gate electrode potential in the reference Hamiltonian

$$H_{\mathrm{ctrl}}(\mathbf{r}, t) = -e_0 \Phi_{\mathrm{ctrl}}(\mathbf{r}, t) = -e_0 \sum_{k=1}^{6} u_k(t)\, \phi_k(\mathbf{r})\,, \tag{11}$$

which will be addressed in more detail in Sec. 4. Throughout this work, the electronic wave packet is always initialized in the adiabatic ground state $\Psi\left(\mathbf{r}, t_i\right) = \Psi_{\text{init}}\left(\mathbf{r}\right)$ at initial time t_i.

In the following, we will frequently use Dirac's notation, which is briefly introduced here for clarity. The corresponding formulation of the TDSE (8)

$$i\hbar|\dot{\Psi}\left(t\right)\rangle = \hat{H}\left(t\right)|\Psi\left(t\right)\rangle, \tag{12}$$

coincides with Eq. (8) after projection on the position basis $\langle\mathbf{r}|\Psi\left(t\right)\rangle = \Psi\left(\mathbf{r}, t\right)$. The Hamiltonian takes the form $\hat{H}\left(t\right) = \hat{H}_0\left(t\right) + \hat{H}_{\text{ctrl}}\left(t\right)$, where the control-related part reads $\hat{H}_{\text{ctrl}}\left(t\right) = -e_0 \sum_{k=1}^{6} u_k\left(t\right) \hat{V}_k$, cf. Eq. (11). Here, $\hat{V}_k$ is a non-dimensionalized control operator, that describes the effect of the k-th gate electrode on the evolution of the electron's wave packet.

3.3 Adiabatic Frame Expansion

In the context of spin-qubit shuttling, a direct solution of the TDSE (8) using split-step methods [40] is only of limited use, as it is challenging to assess whether the evolution is sufficiently adiabatic. Instead, an expansion of the wave packet in instantaneous eigenfunctions of the reference Hamiltonian (*i.e.*, without the control-related part) yields a system for the corresponding complex-valued amplitudes that is directly interpretable. Moreover, this adiabatic frame expansion typically enables an enormous reduction of the system size, since often only a few eigenfunctions are already sufficient. The disadvantage of this approach, however, is that a large number of eigenvalue problems must be solved in a pre-processing step.

The ansatz for the adiabatic frame expansion reads [41]

$$\Psi\left(\mathbf{r}, t\right) = \sum_n c_n\left(t\right) \psi_n\left(\mathbf{r}, t\right), \tag{13}$$

where $c_n\left(t\right) \in \mathbb{C}$ is a complex-valued amplitude and $\psi_n\left(\mathbf{r}, t\right)$ is an instantaneous eigenfunction of the reference Hamiltonian. The corresponding instantaneous eigenvalue problem

$$H_0\left(\mathbf{r}, t\right) \psi_n\left(\mathbf{r}, t\right) = E_n\left(t\right) \psi_n\left(\mathbf{r}, t\right) \tag{14}$$

depends only parametrically on time t. Substitution of Eq. (13) into the TDSE (8) and subsequent projection on an instantaneous eigenstate yields an evolution equation for the amplitudes

$$\begin{aligned} i\dot{c}_n\left(t\right) = \frac{1}{\hbar} E_n\left(t\right) c_n\left(t\right) - i \sum_m \langle\psi_n\left(t\right)|\dot{\psi}_m\left(t\right)\rangle\, c_m\left(t\right) \\ + \frac{1}{\hbar} \sum_m \langle\psi_n\left(t\right)|\hat{H}_{\text{ctrl}}\left(t\right)|\psi_m\left(t\right)\rangle\, c_m\left(t\right). \end{aligned}$$

The sum in the second term is decomposed into the diagonal ($m = n$) and the off-diagonal part, where the latter follows from Eq. (14) via the *Hellmann–Feynman theorem* [41, 42] as

$$\langle\psi_n\left(t\right)|\dot{\psi}_m\left(t\right)\rangle = -\frac{\langle\psi_n\left(t\right)|\dot{\hat{H}}_0\left(t\right)|\psi_m\left(t\right)\rangle}{E_n\left(t\right) - E_m\left(t\right)} \qquad \left(m \neq n\right). \tag{15}$$

By introducing the dynamical phase $\theta_n\left(t\right)$ and the geometric phase $\gamma_n\left(t\right)$

$$\theta_n\left(t\right) = -\frac{1}{\hbar} \int_{t_i}^{t} \mathrm{d}t'\, E_n\left(t'\right), \tag{16}$$

$$\gamma_n\left(t\right) = i \int_{t_i}^{t} \mathrm{d}t'\, \langle\psi_n\left(t'\right)|\dot{\psi}_n\left(t'\right)\rangle, \tag{17}$$

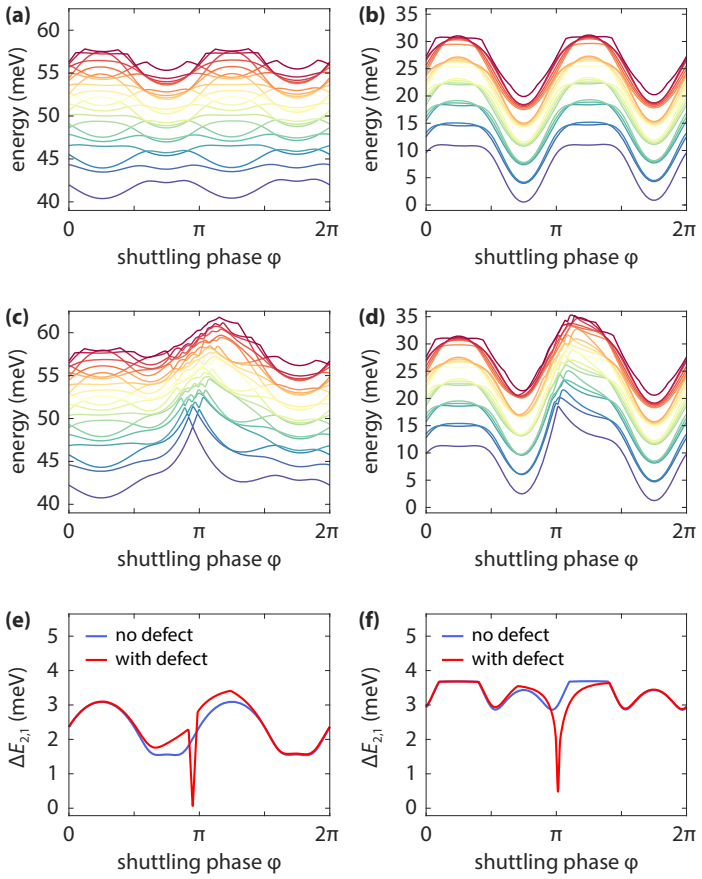

Fig. 4. Energy eigenvalue diagrams of the moving QD as a function of the shuttling phase $\varphi = 2\pi f_s t$. The plot shows the 21 lowest instantaneous energy eigenvalues for different scenarios: **(a)** weak confinement (no charged defect), **(b)** strong confinement (no charged defect), **(c)** weak confinement with charged defect in the QW and **(d)** strong confinement with charged defect in the QW. The negatively charged defect is located near the center of the QW at $\mathbf{r}_0 = (140\,\mathrm{nm}, 1\,\mathrm{nm}, 0\,\mathrm{nm})$, see Appendix B, which corresponds to $\varphi = \pi$. Interaction with the electron is maximal near $\varphi \approx 0.95\,\pi$ in the case of weak confinement and close to $\varphi \approx \pi$ in the strongly confined case. The orbital splitting $\Delta E_{2,1} = E_2 - E_1$ between the ground state and the first excited state is shown for the case of **(e)** weak and **(f)** strong confinement separately. On average, the orbital splitting is about 1 meV smaller in the weakly confined case.

we arrive at

$$
\begin{aligned}
i\dot{c}_n(t) = &-\left(\dot{\gamma}_n(t) + \dot{\theta}_n(t)\right) c_n(t) \\
&+ i \sum_{m \neq n} \frac{\langle \psi_n(t) | \dot{\hat{H}}_0(t) | \psi_m(t) \rangle}{E_n(t) - E_m(t)} c_m(t) \\
&- \frac{e_0}{\hbar} \sum_{k=1}^{6} u_k(t) \sum_m \langle \psi_n(t) | \hat{V}_k | \psi_m(t) \rangle c_m(t)\,.
\end{aligned}
\tag{18}
$$

The first term describes the free evolution according to the energy of the n-th state, the second term describes non-adiabatic transitions between instantaneous eigenstates and the last term represents the effect of the applied control driven by the $u_k(t)$. The effect of the defect potential is entirely contained in the energies and wave functions, which can be significantly modified with respect to the defect-free configuration, see Figs. 4 and 5.

The system (18) can be written compactly in matrix-vector notation

$$i\dot{\mathbf{c}}\left(t\right)=\left(D\left(t\right)+S\left(t\right)+\sum_{k=1}^{6}u_{k}\left(t\right)W^{k}\left(t\right)\right)\mathbf{c}\left(t\right) \tag{19}$$

with Hermitian matrices D, S and W^k. The matrix elements are given as

$$D_{m,n}\left(t\right)=-\dot{\theta}_{n}\left(t\right)\delta_{m,n}=\frac{1}{\hbar}E_{n}\left(t\right)\delta_{m,n}, \tag{20}$$

$$\begin{aligned}W_{m,n}^{k}\left(t\right)&=-\frac{e_{0}}{\hbar}\langle\psi_{m}\left(t\right)|\hat{V}_{k}|\psi_{n}\left(t\right)\rangle \\&=-\frac{e_{0}}{\hbar}\int\mathrm{d}^{3}r\,\psi_{m}^{*}\left(\mathbf{r},t\right)\phi_{k}\left(\mathbf{r}\right)\psi_{n}\left(\mathbf{r},t\right),\end{aligned} \tag{21}$$

$$\begin{aligned}S_{n,n}\left(t\right)&=-\dot{\gamma}_{n}\left(t\right) \\&=-i\int\mathrm{d}^{3}r\,\psi_{n}^{*}\left(\mathbf{r},t\right)\frac{\partial\psi_{n}\left(\mathbf{r},t\right)}{\partial t},\end{aligned} \tag{22}$$

$$\begin{aligned}S_{m,n\neq m}\left(t\right)&=i\frac{\langle\psi_{m}\left(t\right)|\dot{\hat{H}}_{0}\left(t\right)|\psi_{n}\left(t\right)\rangle}{E_{m}\left(t\right)-E_{n}\left(t\right)} \\&=i\hbar\frac{\sum_{k}\dot{U}_{k}\left(t\right)W_{m,n}^{k}\left(t\right)}{E_{m}\left(t\right)-E_{n}\left(t\right)}.\end{aligned} \tag{23}$$

Evaluation of the matrix element (22) always yields zero.

In order to eliminate the rapid phase oscillations from the amplitude dynamics, the system (19) is transformed into a co-rotating frame by means of the rotation matrix

$$R\left(t\right)=\exp\left(-i\int_{t_{i}}^{t}\mathrm{d}t'\,D\left(t'\right)\right). \tag{24}$$

The transformed state vector in the co-rotating frame $\mathbf{C}\left(t\right)=R^{\dagger}\left(t\right)\mathbf{c}\left(t\right)$ obeys the equation of motion

$$i\dot{\mathbf{C}}\left(t\right)=\left(\tilde{S}\left(t\right)+\sum_{k=1}^{6}u_{k}\left(t\right)\tilde{W}^{k}\left(t\right)\right)\mathbf{C}\left(t\right), \tag{25}$$

where the fast oscillations have been transferred to the system matrices $\tilde{S}\left(t\right)=R^{\dagger}\left(t\right)S\left(t\right)R\left(t\right)$ and $\tilde{W}^{k}\left(t\right)=R^{\dagger}\left(t\right)W^{k}\left(t\right)R\left(t\right)$.

3.4 Implementation and Numerical Methods

Prior to the numerical propagation of the amplitude equations (25), the instantaneous eigenvalue problem (14) must be solved with sufficient resolution in the relevant parameter range (*i.e.*, shuttling phase range). In principle, the eigenvalue problem could also be computed on-the-fly during forward propagation, but in view of the numerous forward and backward sweeps that have to be carried out in Sec. 4 for control pulse optimization, it is advantageous to perform this task in a pre-processing step, as it only has to be solved once. Furthermore, this procedure allows to adaptively refine the grid points at which the eigenvalue problem is solved. Details on the employed refinement strategy can be found in Appendix C. The numerically computed eigenvalue curves for different voltage sequences with different QD depths (weak and strong confinement) are shown in Fig. 4 for the situation with and

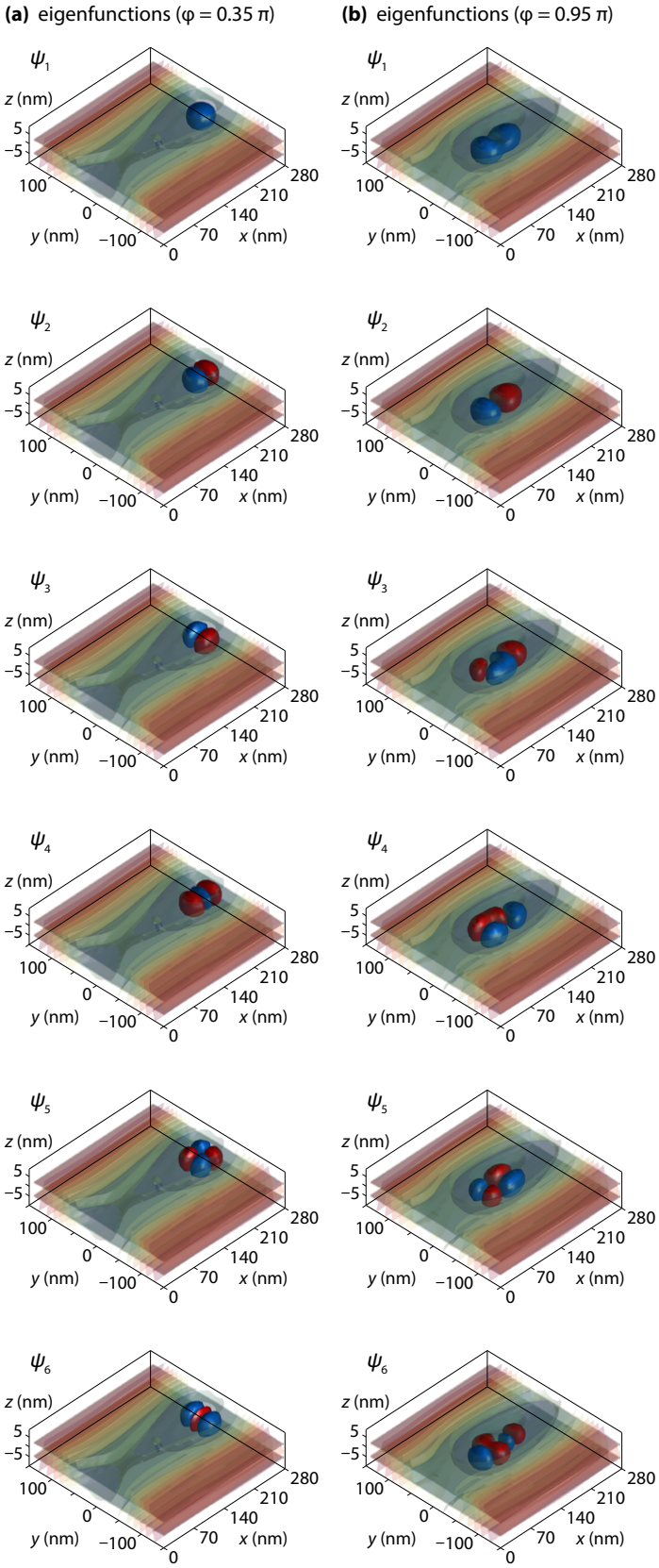

Fig. 5. Isosurface plots of the lowest six orbital eigenfunctions in the weak confinement case, cf. Fig. 4 (c). **(a)** Far away from the defect, at $\varphi = 0.35\,\pi$, the wave functions resemble those of an anisotropic 2D harmonic oscillator (left panel). **(b)** Near the defect, at $\varphi = 0.95\,\pi$, the wave functions are heavily modified (right panel). The wave functions are real-valued and the sign is color-coded (blue positive, red negative).

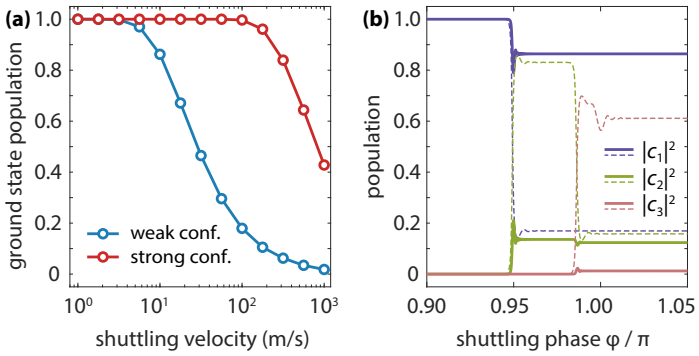

Fig. 6. (a) Ground state occupation probability at the final time after shuttling over one unit cell (four clavier gates) as a function of the shuttling velocity in the case of weak and strong confinement. The device contains a defect in the center of the QW. At sufficiently low shuttling velocity, the electron can bypass the defect without notable population transfer to excited orbital states. At increased velocity, population transfer due to (a sequence of) Landau–Zener transitions leads to a reduction of the ground state population. Using the strong confinement potential, the orbital splitting is increased, such that the Landau–Zener transitions set in only at higher velocities. **(b)** Population dynamics in the case of weak confinement at $v = 10\,\mathrm{m/s}$ (solid, thick) and $v = 100\,\mathrm{m/s}$ (dashed, thin).

without a charged defect in the channel. The parametric family of eigenvalue problems is solved using a matrix-free Lanczos method [43] and a spectral discretization [44] of the stationary Schrödinger operator on a $32 \times 64 \times 16$ grid.

After having resolved all features of the eigenvalue curves (in particular all avoided crossings) with sufficient accuracy, the operators at the corresponding basic grid points are evaluated according to Eqs. (20)–(23). For the dynamical simulation of (25), the matrices are interpolated from these basic grid points onto a temporal grid with a very high resolution. Throughout this work, the time step size is $\Delta t = 50\,\mathrm{fs}$, which according to $\Delta E\,\Delta t = \hbar/2$ allows for the resolution of the dynamics in an energy bandwidth of about $\Delta E \approx 6\,\mathrm{meV}$, cf. Fig. (4). For a target shuttling velocity of around $v_s = 10\,\mathrm{m/s}$ the envelope moves through a unit cell (four clavier gates) of the shuttling device on a time scale of a few $10\,\mathrm{ns}$, such that $10^5 - 10^6$ time steps are required for a full sweep over one unit cell. This reflects the time-scale separation in the current problem, where the time-dependence of the Hamiltonian is much slower than the internal dynamics. At this point, the enormous reduction in system size achieved by the adiabatic frame expansion (in which only the lowest few instantaneous eigenstates are taken into account) pays off, despite the need for the costly pre-processing step. The numerical time stepping scheme is given in Appendix D.

Finally, it is worth noting that the shuttling velocity only enters into the matrix elements (23) in the last step (when interpolating to the fine grid for transient simulation) via the time derivative of the applied voltage. Because of the linear relationship (4) between shuttling phase and frequency, the simulation can be quickly repeated for different shuttling velocities by simple scaling of the system operators (23) without having to solve the series of eigenvalue problems again, see Fig. 6 (a).

3.5 Simulation Results

The dynamics is governed by the eigenvalue curves, see Fig. 4 (a)–(d). For sufficiently slow shuttling speed, the evolution of the electron's wave packet follows the ground state nearly adiabatically if the orbital splitting between the ground state and the first excited state is sufficiently large, cf. Fig. 4 (e)–(f). In the absence of charged impurities in the channel, adiabatic driving is easily achieved for both the weak and the strong confinement mode. The presence of a charged defect, however, results in substantial modifications of the energy diagrams, see Fig. 4. In the case of the negative point charge studied

in this paper, the defect can effectively split the QD into a double QD, in which the ground state and the first excited state can become very close in energy. This manifests itself in an avoided eigenvalue crossing, see Fig. 4, where the energy gap (*i.e.*, the orbital splitting) becomes very small for a short time. Subsequently, this triggers a Landau–Zener transition in which the electron transitions into an excited state with a high probability after passing over the defect. The probability of the Landau–Zener transition scales exponentially with the shuttling speed [37, 45]. As there is a large number of avoided eigenvalue crossings in the vicinity of the defect, this can easily initiate a sequence of Landau–Zener transitions to even higher excited states. This behavior is reflected in the simulation results depicted in Fig. 6 (a), where the probability of ground state occupation after passing through the defect is shown as a function of the shuttling velocity. While the ground state occupation in the weak confinement mode is already clearly reduced at around $v_s = 10\,\mathrm{m/s}$, the deeper QDs in the strong confinement mode can still pass the same defect without disturbance at a 10 times higher speed. The population dynamics is shown in Fig. 6 (b) for the case of the weak confinement potential at two different shuttling velocities. In the case of the high shuttling velocity ($v_s = 100\,\mathrm{m/s}$), cascades of Landau–Zener transitions occur, which would be detrimental for quantum information transfer. After the Landau–Zener transition, the electron is in a coherent superposition of several eigenstates, which potentially offer numerous stochastic decay channels. As an indicator of this, we will monitor the energy uncertainty of the transported electron in the following, which is significantly increased after passing over the defect.

4 Quantum Optimal Control

Charged defects can trigger population transfer to excited orbital states in a sequence of Landau–Zener transitions. As a consequence, the electron's effective g-factor is then modified with respect to the ground state due to the different spatial extension of the orbital wave function [46, 47]. This results in a modification of the spin-precession in the external magnetic field such that the spin accumulates an additional phase. Electron-phonon interaction finally drives the relaxation of the electron back to the ground state [21, 48, 49]. As the relaxation process is stochastic in nature, this leads to a randomization of the accumulated phase and thus to spin-dephasing. Although this process can be mitigated either by adaptive regulation of the shuttling speed or by increasing the QD confinement depth, these approaches have disadvantages either with regard to the synchronization of the qubit shuttle with other functional units on the chip or can promote heating due to the increased electrical power. As an alternative, we investigate how the screening gates can be employed to optimally circumvent such defect centers in order to achieve a high transfer fidelity without reducing the shuttling speed.

In the following, we seek to optimize control voltage pulses $u_k\,(t)$ that allow for a quasi-adiabatic passage of the electron through the channel in the presence of a charged defect. The problem is related to scenarios where *counterdiabatic driving* [50] can be employed, it is however complicated because the control itself decisively changes the potential landscape and thus modifies the electronic state space.

4.1 Cost Functional

The computation of optimal control pulses $u_k\,(t)$ is based on the minimization of a cost functional that captures the objective of the optimization. The choice of a suitable cost function is therefore crucial and must be considered carefully.

In the present scenario, we seek to steer the electron around a charged defect in a quasi-adiabatic

fashion. We thus strive for a control signal that is effective only for a short period of time and fades out again after passing by the defect. Accordingly, the electron should travel adiabatically in the ground state of the uncontrolled Hamiltonian $\hat{H}_0(t)$ before and after the passage of the critical region. A first candidate for the cost functional could thus target the maximization of the ground state occupation at the end of the considered time interval. Since this objective, however, can also be reached after passing through a sequence of Landau–Zener transitions by a specific operation only at the end of the time window, it becomes clear that a running cost functional that quantifies the properties of the electron during shuttling should be employed instead. Naively, this suggests to minimize the accumulated energy expectation value of the electron with respect to the uncontrolled Hamiltonian over the considered time interval, in order to enforce adiabatic following of the ground state energy branch. This ansatz, however, disregards the additional control term (9) in the full Hamiltonian, which describes the change of the potential landscape in which the electron is conveyed. The next conceivable idea would therefore be to minimize the energy with respect to the full Hamiltonian including the applied control. This ansatz for the cost functional, however, also proves to be unsuitable without further restrictions on the control amplitudes, as this objective could be reached by arbitrarily strong deepening of the QD potentials.

Instead, minimization of the energy uncertainty with respect to the full Hamiltonian $\hat{H}(t) \equiv \hat{H}(t, \mathbf{u}(t))$ turns out to be a suitable cost functional, since it precisely captures the primary goal of achieving a maximally deterministic passage of the electron through the channel. The cost functional

$$J(\Psi, \mathbf{u}) = \frac{1}{\hbar E_{\mathrm{ref}}} \int_{t_i}^{t_f} \mathrm{d}t \; \mathrm{Var}_{\Psi(t)} \left(\hat{H}(t, \mathbf{u}(t)) \right) \tag{26}$$

accumulates the variance of the electron's energy with respect to the full Hamiltonian

$$\begin{aligned} \mathrm{Var}_{\Psi(t)} \left(\hat{H}(t, \mathbf{u}(t)) \right) = \langle \Psi(t) | \hat{H}^2(t, \mathbf{u}(t)) | \Psi(t) \rangle \\ - \langle \Psi(t) | \hat{H}(t, \mathbf{u}(t)) | \Psi(t) \rangle^2 \end{aligned} \tag{27}$$

in the considered time interval $[t_i, t_f]$. As a dynamical constraint, the state vector $|\Psi(t)\rangle$ must obey the TDSE (12) at any time, which depends on the control pulses $\mathbf{u}(t)$ via the Hamiltonian $\hat{H}(t) \equiv \hat{H}(t, \mathbf{u}(t))$. The theoretical minimum $J = 0$ corresponds to an electron that is conveyed in the ground state of the controlled Hamiltonian (since eigenstates have a sharply defined energy). Minimization of Eq. (26) thus allows to determine the control pulses $u_k(t)$, the trajectory of the wave packet and the corresponding Hamiltonian as generator of the evolution in a self-consistent way. For a finite control pulse width, the aforementioned objectives (entering and leaving the critical region in the ground state of the uncontrolled Hamiltonian) are automatically met. Note that the cost functional does not include any further restrictions on the control pulse amplitudes. The cost functional (26) is non-dimensionalized by scaling with the reference energy $E_{\mathrm{ref}} = 2\pi\hbar f_s$.

4.2 Pontryagin's Maximum Principle

The cost functional (26) is to be minimized while taking the TDSE (12) as a dynamic side constraint into account. Using the Lagrange multiplier method, this constrained optimization problem is turned into an unconstrained optimization problem, which targets the minimization of the augmented cost functional [51, 52]

$$\begin{aligned} \tilde{J}(\Psi, \mathbf{u}, \chi) = J(\Psi, \mathbf{u}) \\ + \frac{2}{\hbar} \mathrm{Im} \int_{t_i}^{t_f} \mathrm{d}t \, \langle \chi(t) | \Big(\hat{H}(t, \mathbf{u}(t)) | \Psi(t) \rangle - i\hbar | \dot{\Psi}(t) \rangle \Big). \end{aligned} \tag{28}$$

Here, the bra-state $\langle\chi\,(t)\,|$ is a time-dependent Lagrange multiplier, which enforces the dynamical side constraint. The key purpose of the Lagrange multipliers is to facilitate the evaluation of the gradient of the cost functional with respect to the controls $u_k\,(t)$. The gradient is required for the minimization procedure described below.

Following Pontryagin's maximum principle [52], we consider the variation of Eq. (28) with respect to all variables in order to obtain a set of necessary conditions characterizing a local minimum. Evaluation of the Gâteaux derivative

$$\delta\tilde{J}\,(\Psi,\mathbf{u},\chi)=\lim_{\epsilon\to 0}\frac{\tilde{J}\,(\Psi+\epsilon\,\delta\Psi,\mathbf{u}+\epsilon\,\delta\mathbf{u},\chi+\epsilon\,\delta\chi)-\tilde{J}\,(\Psi,\mathbf{u},\chi)}{\epsilon}$$

yields

$$\begin{aligned}\delta\tilde{J}\,(\Psi,\mathbf{u},\chi)=\delta J\,(\Psi,\mathbf{u})&\\+\frac{2}{\hbar}\,\mathrm{Im}\int_{t_i}^{t_f}\mathrm{d}t\,\langle\delta\chi\,(t)\,|\,\Big(\hat{H}\,(t,\mathbf{u}\,(t))\,|\Psi\,(t)\rangle-i\hbar|\dot{\Psi}\,(t)\rangle\Big)&\\-\frac{2}{\hbar}\,\mathrm{Im}\int_{t_i}^{t_f}\mathrm{d}t\,\langle\delta\Psi\,(t)\,|\,\Big(\hat{H}\,(t,\mathbf{u}\,(t))\,|\chi\,(t)\rangle-i\hbar|\dot{\chi}\,(t)\rangle\Big)&\\-2\,\mathrm{Re}\,(\langle\delta\Psi\,(t_f)\,|\chi\,(t_f)\rangle)+2\,\mathrm{Re}\,(\langle\delta\Psi\,(t_i)\,|\chi\,(t_i)\rangle)&\\+\sum_{k=1}^{6}\int_{t_i}^{t_f}\mathrm{d}t\,\frac{2}{\hbar}\,\mathrm{Im}\,\Big(\langle\chi\,(t)\,|\hat{V}_k\,(t)\,|\Psi\,(t)\rangle\Big)\,\delta u_k\,(t)\,.&\end{aligned}$$

This step includes the functional derivative of the cost functional (26), which is obtained as

$$\begin{aligned}\delta J\,(\Psi,\mathbf{u})=\frac{2}{\hbar}\,\mathrm{Im}\int_{t_i}^{t_f}\mathrm{d}t\,\langle\delta\Psi\,(t)\,|i\hbar\mathrm{D}_{\langle\Psi(t)|}J\,(\Psi,\mathbf{u})&\\+\sum_{k=1}^{6}\int_{t_i}^{t_f}\mathrm{d}t\,\mathrm{D}_{u_k(t)}J\,(\Psi,\mathbf{u})\;\delta u_k\,(t)&\end{aligned}$$

with

$$\begin{aligned}\mathrm{D}_{\langle\Psi(t)|}J\,(\Psi,\mathbf{u})=\frac{1}{\hbar E_{\mathrm{ref}}}\Big(\hat{H}^2\,(t,\mathbf{u}\,(t))\,|\Psi\,(t)\rangle&\\-2\langle\Psi\,(t)\,|\hat{H}\,(t,\mathbf{u}\,(t))\,|\Psi\,(t)\rangle\,\hat{H}\,(t,\mathbf{u}\,(t))\,|\Psi\,(t)\rangle\Big),&\end{aligned}\tag{29a}$$

$$\begin{aligned}\mathrm{D}_{u_k(t)}J\,(\Psi,\mathbf{u})=\frac{2}{\hbar E_{\mathrm{ref}}}\,\mathrm{Re}\,\Big(\langle\Psi\,(t)\,|\hat{H}\,(t,\mathbf{u}\,(t))\,\hat{V}_k|\Psi\,(t)\rangle&\\-\langle\Psi\,(t)\,|\hat{H}\,(t,\mathbf{u}\,(t))\,|\Psi\,(t)\rangle\,\langle\Psi\,(t)\,|\hat{V}_k|\Psi\,(t)\rangle\Big).&\end{aligned}\tag{29b}$$

The wave packet is always initialized in the instantaneous ground state, such that $|\delta\Psi\,(t_i)\rangle=0$. With this, a local minimum, for which $\delta\tilde{J}\,(\Psi,\mathbf{u},\chi)=0$, is characterized by:

1 The initial value problem for the state evolution

$$i\hbar|\dot{\Psi}\,(t)\rangle=\hat{H}\,(t,\mathbf{u}\,(t))\,|\Psi\,(t)\rangle,\tag{30a}$$

$$|\Psi\,(t_i)\rangle=|\Psi_{\mathrm{init}}\rangle\tag{30b}$$

to be solved forward in time. The evolution of the state vector $|\Psi\,(t)\rangle$ is uniquely prescribed for given controls $\mathbf{u}\,(t)$ and initial data $|\Psi_{\mathrm{init}}\rangle$.

2 The final value problem for the co-state evolution (inhomogeneous TDSE)

$$i\hbar|\dot{\chi}\left(t\right)\rangle = \hat{H}\left(t,\mathbf{u}\left(t\right)\right)|\chi\left(t\right)\rangle - i\hbar \mathrm{D}_{\langle\Psi(t)|}J\left(\Psi,\mathbf{u}\right) \tag{31a}$$

$$|\chi\left(t_f\right)\rangle = \frac{\partial J\left(\Psi,\mathbf{u}\right)}{\partial\langle\Psi\left(t_f\right)|} = 0 \tag{31b}$$

to be solved backward in time. Since the cost functional (26) is a fourth-order polynomial in the free variables Ψ and $\mathbf{u}$, the resulting driving term (29a) in the inhomogeneous TDSE is of third order. Note that this inhomogeneous term involves single and twofold application of the Hamiltonian on the state vector as well as the running energy expectation value $\langle\Psi\left(t\right)|\hat{H}\left(t,\mathbf{u}\left(t\right)\right)|\Psi\left(t\right)\rangle$. The co-state value at final time is zero $|\chi\left(t_f\right)\rangle = 0$, because the cost functional does not explicitly depend on the final state $|\Psi\left(t_f\right)\rangle$.

3 The optimality conditions

$$\mathrm{D}_{u_k}\tilde{J}\left(\Psi,\mathbf{u},\chi\right) = \frac{2}{\hbar}\,\mathrm{Im}\left(\langle\chi\left(t\right)|\hat{V}_k\left(t\right)|\Psi\left(t\right)\rangle\right) + \mathrm{D}_{u_k}J\left(\Psi,\mathbf{u}\right) = 0, \tag{32}$$

which characterize a (locally) optimal control by vanishing gradients.

The gradients $\mathrm{D}_{u_k}\tilde{J}\left(\Psi,\mathbf{u},\chi\right)$ give a descent direction that is used in gradient-based minimization methods. The simplest approach is the gradient descent method, in which, after solving the forward and backward equations (30)–(31) for a given control $\mathbf{u}^{(j)}\left(t\right)$ in the j-th step of the iteration, an improved control $\mathbf{u}^{(j+1)}\left(t\right)$ is found via

$$u_k^{(j+1)}\left(t\right) = u_k^{(j)}\left(t\right) - \alpha^{(j)}\mathrm{D}_{u_k}\tilde{J}\left(\Psi^{(j)}\left(t\right),\mathbf{u}^{(j)}\left(t\right),\chi^{(j)}\left(t\right)\right). \tag{33}$$

Here, $\alpha^{(j)} > 0$ is a step size that has to be determined via a line search method [53] such that the cost functional is decreased sufficiently: $J\left(\Psi^{(j+1)},\mathbf{u}^{(j+1)}\right) < J\left(\Psi^{(j)},\mathbf{u}^{(j)}\right)$. The simple gradient descent method [54], however, does not contain any information on the curvature of the cost functional and thus convergence stagnates when approaching the minimum. Therefore, a quasi-Newton method with superlinear convergence is employed in this work. Specifically, we employ the L-BFGS method [53], where the above update rule (33) is modified by an approximate inverse Hessian, that is recursively computed from the gradients and step sizes of previous iterations. This approach has been previously employed in quantum optimal control [55] and is indispensable for handling the typically rapidly oscillating updates provided by the gradient in the current problem. Next to L-BFGS, we have also tested the Barzilai–Borwein method [56], which is easily implemented and does not require any line search. We likewise achieved useful results with this method, but retained L-BFGS due to the faster convergence.

4.3 Control Pulse Optimization

Direct optimization of the control pulses $\mathbf{u}\left(t\right)$ as a free-shape function of time is challenging as the gradient (32) typically yields rapidly oscillating updates which impedes convergence to a pulse-like control signal. Although we managed to achieve pulse-like controls in some cases by carefully selecting suitable initial pulses and adding further constraints on the amplitude and spectrum of the control [57], the signals obtained in this way appeared to be impractical for experimental realization.

Consequently, we restrict the functional form of the control signals in the following to Lorentzian-shaped pulses

$$u_k\left(t\right) = A_k\,\frac{T_k^2}{\left(t-t_{0,k}\right)^2 + T_k^2}, \qquad k = 1\ldots 6, \tag{34}$$

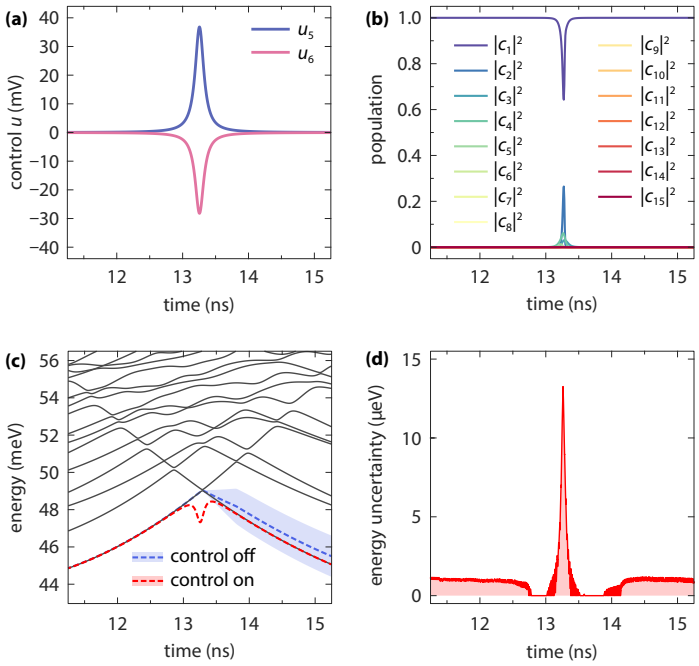

Fig. 7. Results of the multi-parameter optimization routine. **(a)** Optimized Lorentzian-shaped screening gate pulses. The pulse is centered at $t_0^* = 13.26\,\mathrm{ns}$ and the pulse width is $T^* = 78.8\,\mathrm{ps}$. The amplitudes are $A_5^* \approx -28.2\,\mathrm{mV}$ and $A_6 \approx +36.8\,\mathrm{mV}$. **(b)** Amplitude dynamics of the wave packet under optimal control. The wave function is expanded in eigenstates of the (uncontrolled) reference Hamiltonian (10) to approximate the instantaneous ground state of the controlled problem. Near the avoided crossing, significant contributions from excited orbital eigenstates are employed to build up the wave packet. With the optimal control in place, the wave packet enters and leaves the critical region in the ground state of the uncontrolled problem with probability practically equal to one. **(c)** Expectation value and standard deviation of electron's energy with (red) and without (blue) screening gate control. The electron is initialized in the ground state and shuttles with $v = 10\,\mathrm{m/s}$ toward the defect. Without control, the electron is in a superposition state after passing over the defect and therefore has a significant energy uncertainty of about $\Delta E \approx 1\,\mathrm{meV}$ (light blue shade). The control pulse is optimized to minimize the running energy uncertainty and takes a route below the ground state energy branch in the critical region in the energy diagram. This corresponds to a precisely tuned lateral shift of the electron via the screening gates, that suppresses the Landau–Zener transition and keeps the electron in the ground state of the controlled Hamiltonian. **(d)** The energy uncertainty is reduced to about $\Delta E \approx 1\,\mu\mathrm{eV}$ with a short peak of about $\Delta E \approx 13\,\mu\mathrm{eV}$ in the vicinity of the defect. The energy uncertainty is invisibly small in panel (c).

and limit ourselves to the optimization of the pulse parameters (amplitude A_k, pulse width T_k and peak time $t_{0,k}$). Next to Lorentzian-shaped pulses we have also tested different envelope functions (Gaussian, sech, triangle) and obtained comparable results. The choice of the pulse envelope shape therefore does not seem to be too restrictive.

The optimization problem formulated in Sec. 4.2 must be adapted by substituting $u_k(t) \to u_k(t, \mathbf{p})$, where the vector $\mathbf{p}$ contains all free parameters of the pulse (34). The gradient of the augmented cost functional with respect to the parameters $\mathbf{p}$ then follows via the chain rule as

$$\nabla_{\mathbf{p}} \tilde{J}(\Psi, \mathbf{u}, \chi) = \sum_{k=1}^{6} \int_{t_i}^{t_f} \mathrm{d}t\, \mathrm{D}_{u_k} \tilde{J}(\Psi(t), \mathbf{u}(t, \mathbf{p}), \chi(t))\, \nabla_{\mathbf{p}} u_k(t, \mathbf{p}), \tag{35}$$

which is used as a descent direction in the quasi-Newton method.

In the following, we optimize the parameters of the control pulses $u_{5,6}(t)$ applied at the screening gates (*i.e.*, no correction pulses are applied to the clavier gates). We keep the pulse width and the peak time identical for both pulses, but allow for unequal amplitudes. A quasi-Newton method is employed to optimize the parameter set $\mathbf{p} = (t_0, T, A_5, A_6)$. The method converges superlinearly and minimizes

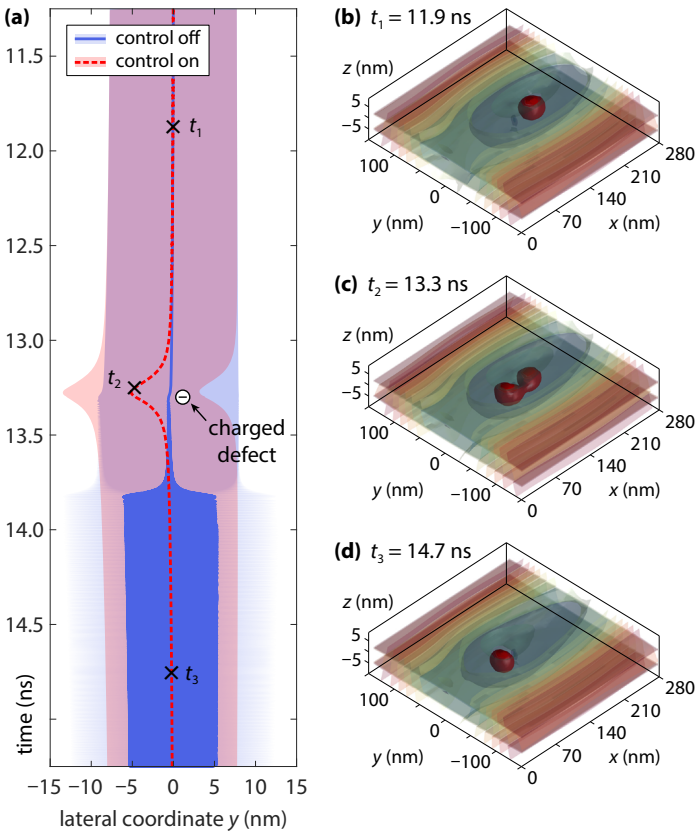

Fig. 8. (a) Expectation value and standard deviation of the lateral coordinate $\langle y\,(t)\rangle = \langle\Psi\,(t)\,|\hat{y}|\Psi\,(t)\rangle$ as a function of time. Optimal control conveys the wave packet back to the central shuttling line after bypassing the defect (red line). Without control, the wave packet's lateral position oscillates rapidly within the QD after interaction with the defect (blue line). **(b)–(d)** Snapshots of the electron's orbital wave function before, during and after passage of the defect.

the accumulated energy uncertainty (*i.e.*, the cost functional) for $t_0^* \approx 13.26\,\text{ns}$, $T^* = 78.8\,\text{ps}$, $A_5^* = -36.8\,\text{meV}$ and $A_6^* \approx +28.2\,\text{meV}$. The corresponding pulses are shown in Fig. 7 (a). As above, the electronic wave function is still expanded in the instantaneous eigenbasis of the uncontrolled Hamiltonian $\hat{H}_0\,(t)$. The evolution of the absolute values of the amplitudes is shown in Fig. 7 (b). Indeed, one observes the desired behavior: Before and after passage of the critical region, the electron occupies exclusively the ground state of the uncontrolled Hamiltonian. In order to circumvent the defect, however, excited states are temporarily occupied in order to approximate the instantaneous ground state of the *controlled* Hamiltonian. The corresponding wave function is laterally shifted along the y-direction as we will see below. The figure shows that already about 15 eigenfunctions of (10) are sufficient to approximate the orbital ground state of the controlled system. The computation was repeated with a larger number of states, but the results remain almost unchanged. The evolution of the energy expectation value and the energy uncertainty (standard deviation) of the electron during shuttling are shown in Fig. 7 (c). Without control, the electron is swept through a Landau–Zener transition at the defect and subsequently has an average energy expectation value well above the instantaneous ground state. The energy uncertainty is increased to about $\Delta E \approx 1\,\text{meV}$ after passing over the defect. By switching on the optimized control pulses at the screening gates, the energy expectation value closely follows the instantaneous ground state before and after the passing through the critical region. In the vicinity of the defect, the energy expectation value is decreased below the ground state energy of the uncontrolled Hamiltonian. Here, the unequal amplitudes A_5 and A_6 do not only lead to a lateral shift of the QD, but also temporarily modify the QD confinement, which corresponds to the short-term decrease of the energy expectation value. The evolution of the corresponding energy uncertainty is shown in

Fig. 7 (d): In the vicinity of the defect, the energy uncertainty shortly peaks at about $\Delta E \approx 13\,\mu\text{eV}$, but before and after this point the value is very small, $\Delta E \approx 1\,\mu\text{eV}$. The electron-wave packet hence quasi-adiabatically follows the ground state of the controlled Hamiltonian.

Finally, Fig. 8 shows the trajectory of the y-component of the geometric barycenter $\langle y\,(t)\rangle = \langle \Psi\,(t)\,|\hat{y}|\Psi\,(t)\rangle$ of the wave packet. Without the optimized control pulses, the wave packet flickers erratically from side to side within the QD after passing through the defect. This behavior is to be expected, as the electron here is essentially in a superposition of an s-type and a p-type orbital, cf. Fig. 5 and Fig. 6 (b), and the associated complex amplitudes exhibit rapid oscillation (outside the co-rotating frame). Under the action of the optimized control, the electron is guided past the charged defect at a safe distance and is then smoothly conveyed back to the central shuttling line, see Fig. 8 (a). The width of the wave packet remains practically invariant during this process.

In summary, the results indicate that a quasi-adiabatic evolution of the electron wave packet can already be achieved with a very simple pulse shape (34) and that the Si-QuBus is capable of compensating for the effect of charged defects by properly calibrated screening gate pulse sequences. On the one hand, the defect under consideration is nearly a worst-case scenario due to its central location near the center of the QW. On the other hand, the situation can be considered generic and we assume that equivalent results can be achieved for other defect types and locations.

4.4 Impact of the Control Pulse in a Defect-Free Segment of the Channel

It is intended to shuttle multiple electrons simultaneously in different QDs of the Si-QuBus. Note that loading and shuttling of patterns with up to 34 electrons has already been demonstrated in Ref. [25]. Since the use of only six individually controllable gate electrode sets (four clavier gates, two screening gates, see Fig. 1) is crucial for the scalability of the device, the control pulse described above might also affect electrons located in other segments of the channel. It is clear that these electrons should not experience orbital excitations in response to the control pulse.

We investigate the impact of the optimized control pulse on an electron shuttling through a defect-free segment of the channel (shifted by a multiple of L_x in propagation direction), see Fig. 4 (a) for the corresponding energy diagram. Everything else (in particular, the weak confinement voltages) is kept unchanged. The results are illustrated in Fig. 9. The control pulse temporarily shifts the lateral coordinate of the electron by a few nm and reduces the confinement energy in comparison to the uncontrolled case. The electron, however, returns to the central shuttling line and the nominal ground state energy without notable signatures of the control. The energy uncertainty accumulated in this process is negligible. Finally, we note that in the special case of only a single relevant charged defect in a shuttle segment, *i.e.*, a lane confined by one long screening gate segment, the defect might be avoided by simply adjusting the DC voltages applied to the screening gates. Hence, no voltage pulse would be required in this case.

The concept of tailoring correcting pulses to minimize the impact of (charged) defects in the device is thus compatible with the scalability requirements of the Si-QuBus. In the simulations, this was demonstrated for the weak confinement mode, where the orbital splitting is about $1.5 - 3.0\,\text{meV}$ across the channel. For enlarged orbital splitting (*e.g.*, in the strong confinement mode considered above), the effect should be even smaller.

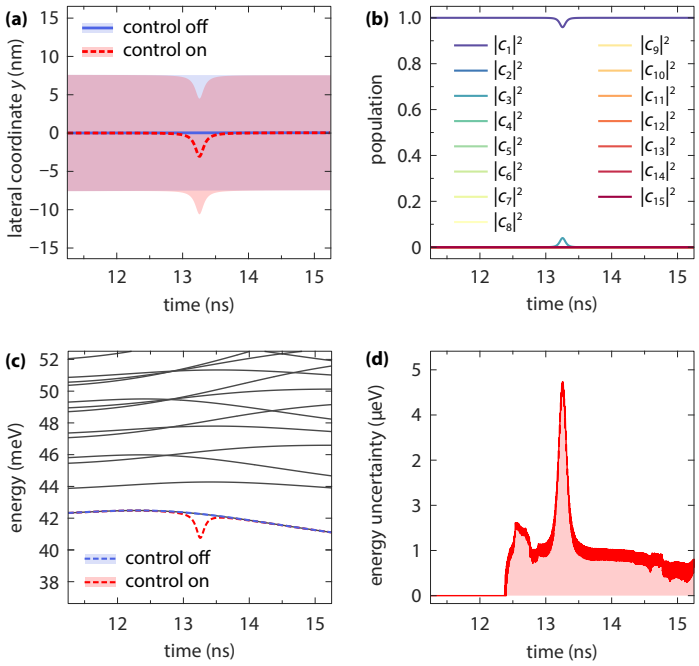

Fig. 9. Impact of the control pulse on an electron in a defect-free segment of the channel. **(a)** Dynamics of the y-coordinate without (blue line) and with (red line) the optimized control pulse. The control induces a short-term lateral shift of the electron's position, but conveys it back smoothly to the central shuttling line. **(b)** Evolution of expansion coefficients of the wave function under control. The electron is returned to the adiabatic ground state after exposure to the control pulse. **(c)** The energy expectation value is temporarily reduced with respect to the adiabatic ground state during the pulse, but returns back to the ground state afterwards, cf. Fig. 7 (c). The corresponding energy uncertainty shown in **(d)** is very small throughout the considered time interval.

5 Summary and Discussion

The simulation-based analysis of the controllability of the Si-QuBus shows that it is possible to bypass charged impurities in the channel via precisely tuned control pulses. Already very simple pulse shapes allow to realize a quasi-adiabatic evolution of the wave packet, which is characterized by a very small energy uncertainty during shuttling. While the control is expected to cause local modifications of the effective g-factor of the electron due to a change of its trajectory, it is important to point out that these modifications can be made practically deterministic. Therefore, also the accumulated spin-phase should be deterministic, which can be taken into account in further qubit-processing. Moreover, as the control steers the electron in the ground state of the dynamically adapted potential landscape, no new dissipation channels should arise. In order to mitigate unintentional heating effects, we have optimized for the pulse with the smallest admissible amplitudes.

The key problem for applying the optimal control strategy presented above in real experiments is that the employed open loop control theory requires complete knowledge of the defect landscape in the shuttling channel. While shuttling tomography experiments allow to draw certain conclusions about the location of defects in the channel [25], exact mapping is a difficult inverse problem and will be hard to achieve. On the other hand, we have demonstrated that already simple control pulse shapes with a few parameters can yield good results. The theoretical investigation presented here could therefore be used as a guideline to implement the respective controls in experiments with the help of a suitable feedback loop.

For electron spin-qubits in Si considered in this work, we note that the orbital excitation considered here is not the main limitation. Excited orbital states exhibit a tiny deviation from the orbital ground state

and orbital relaxation is fast [21]. Typically, the shuttling velocity is limited by inter-valley transitions triggered by atomic-scale alloy fluctuations at the Si/SiGe QW interface. Meanwhile, several strategies have been developed that might lead to a deterministic enhancement of the valley splitting [33, 58–60]. Consequently, orbital excitations triggered by charged defects, whose effects can be mitigated by suitable control pulses as described above, could become the relevant bottleneck at increased shuttling velocities.

Similarly, our results might be highly relevant for hole qubits, *e.g.*, in Ge/SiGe, for which the issue of the valley degeneracy is absent. For holes, the spin-orbital interaction is dominant [61]. As a consequence, stochastic orbital excitations and relaxations induce qubit dephasing due to the large variations of hole g-tensor across orbitals. The spin-orbit relaxation rate is enhanced opening up a dangerous spin-relaxation channel triggered by orbital excitations. Especially at a high shuttling velocity, abrupt changes in the electrostatic potential as considered here and thus orbital excitations are a major bottleneck for hole spin-qubits.

In summary, we have presented a comprehensive modeling approach for the simulation of single-electron shuttling in the Si-QuBus using a multi-dimensional device model with realistic gate electrode potentials. We investigated the orbital excitation dynamics of an electron that is captured in a moving QD and swept across a single negatively charged defect for different choices of the QD confinement parameters and the shuttling velocity. The main contribution of this work is the study of an engineered control voltage pulse that is tailored to circumvent a charged defect in a deterministic manner in order to maintain adiabaticity during shuttling. Quantum optimal control theory was employed to optimize the control pulse parameters via minimization of the accumulated energy uncertainty during shuttling. Our results indicate that already simple pulse shapes characterized by a few parameters enable a practically deterministic passage of charged defects within the channel. The control pulse should thus prevent the spin-qubit from dephasing. Finally, we demonstrated the compatibility of the control strategy with the scalability requirements of the Si-QuBus.

A Geometry and Parameters

The geometry of a unit cell of the Si-QuBus is shown in Fig. 10, where the geometry parameters are indicated. The corresponding parameter values are listed in Tab. 2. A complete list of material parameter entering the Poisson problem and the Schrödinger equation is given in Tab. 3.

B Charged Defect Potential

We consider a negatively charged point defect located at $\mathbf{r}_0 = (x, y, z) = (140\,\text{nm}, 1\,\text{nm}, 0\,\text{nm})$ which disturbs the evolution of the shuttled electron. The corresponding electrostatic energy in the Hamiltonian (10) is $V_{\text{defect}}(\mathbf{r}) = -e_0\Phi_{\text{defect}}(\mathbf{r})$, where $\Phi_{\text{defect}}(\mathbf{r})$ solves the Poisson problem

$$\begin{aligned} -\nabla\cdot\left(\varepsilon(\mathbf{r})\,\nabla\Phi_{\text{defect}}(\mathbf{r})\right) &= -e_0\delta(\mathbf{r}-\mathbf{r}_0)\\ \Phi_{\text{defect}}(\mathbf{r})\,|_{\Gamma_{k=1\ldots6}} &= 0,\\ \mathbf{n}\cdot\nabla\Phi_{\text{defect}}(\mathbf{r})\,|_{\Gamma_N} &= 0,\\ \Phi_{\text{defect}}(\mathbf{r})\,|_{\Gamma_{\text{period}}} &= \Phi_{\text{defect}}(\mathbf{r}+\mathbf{e}_x L_x)\,. \end{aligned} \tag{36}$$

The defect potential landscape thus takes the effects of the layered heterostructure and the gate electrodes into account. The potential therefore differs from a simple $1/r$ potential.

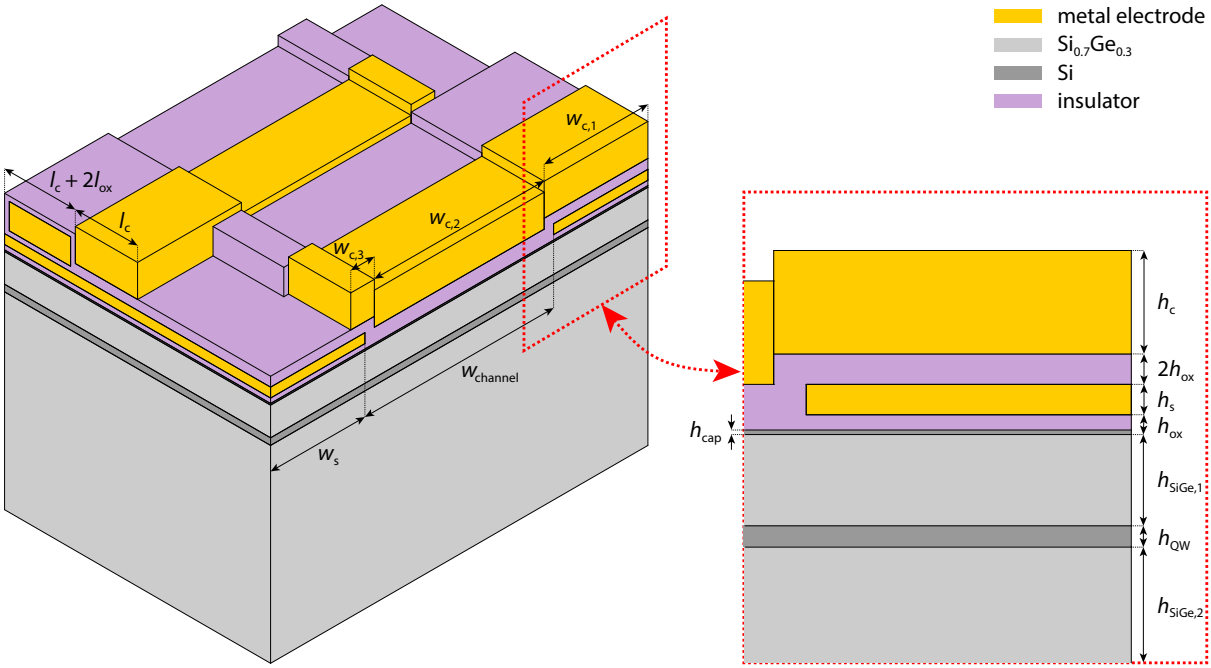

Fig. 10. Schematic illustration of the device geometry

symbol	description	value
h_c	height of clavier gate	34 nm
h_{ox}	height of oxide layer	5 nm
h_s	height of screening gate	10 nm
h_{cap}	thickness of Si cap layer	1.5 nm
$h_{SiGe,1}$	thickness of SiGe barrier above QW	30 nm
h_{QW}	quantum well layer thickness	7 nm
$h_{SiGe,2}$	thickness of SiGe substrate	1000 nm
l_c	clavier gate length	65 nm
l_{ox}	thickness of insulator	5 nm
l_g	gate pitch $l_g = l_c + l_{oc}$	70 nm
L_x	length of a unit cell $L_x = 4l_g$	280 nm
$w_{c,1}$	width of clavier gate segment	100 nm
$w_{c,2}$	width of central clavier gate segment	180 nm
$w_{c,3}$	width of clavier gate segment	20 nm
w_s	width of screening gate	100 nm
$w_{channel}$	channel width $w_{channel} = w_{c,2} + 4l_{ox}$	200 nm

Tab. 2. Geometry parameters.

C Recursive Refinement of Eigenvalue Sweep Resolution and Wave Function Alignment

The instantaneous eigenvalue problem (14) is solved in a pre-processing step over a predefined range of the shuttling phase $\varphi \in [\varphi_i, \varphi_f]$. In Fig. 4, the eigenvalue curves were computed over one unit cell $\varphi \in [0, 2\pi]$.

symbol	description	value
$\varepsilon_r\,(\mathrm{Si})$	dielectric permittivity of Si	12
$\varepsilon_r\,(\mathrm{SiGe})$	dielectric permittivity of $Si_{0.7}Ge_{0.3}$	13.2
$\varepsilon_r\,(\mathrm{insulator})$	dielectric permittivity of the insulator	6
m_e^*	effective electron mass [62], same for Si and $Si_{0.7}Ge_{0.3}$	$0.19\,m_0$
ΔE_c	QW conduction band offset [62]	124 meV

Tab. 3. Material parameters.

As the eigenvalue problem (14) is invariant under transformations of the phase of the eigenfunctions, the latter are not uniquely determined from the numerical solution. Instead, the eigenfunctions must be aligned such that they change smoothly along the eigenvalue branches under continuous change of the parameter φ (or time). As the Hamiltonian is real-valued throughout, the wave functions can be chosen real as well. Thus, the phase-invariance reduces to a free sign $\psi_n(\mathbf{r},t) \leftrightarrow -\psi_n(\mathbf{r},t)$. In order to align the signs of the eigenfunctions, we consider the overlap of successive eigenfunctions on the same eigenvalue branch

$$\langle \psi_n(t_j) \,|\psi_n(t_{j+1})\rangle > 0, \tag{37a}$$

which is required to be positive. If the condition (37a) is violated, the sign of the latest wave function is swapped $\psi_n(\mathbf{r},t_{j+1}) \to -\psi_n(\mathbf{r},t_{j+1})$. Far away from avoided crossings, where eigenfunctions preserve their character along the branch, the modulus of the overlap is usually close to unity for reasonable step sizes, such that the decision for sign swaps is easily made. In the vicinity of avoided crossings, however, the overlap between successive eigenfunctions on the same branch can become very small as the eigenfunctions quickly change their character. Therefore, a second criterion on the magnitude of the overlap integral is introduced

$$|\langle \psi_n(t_j) \,|\psi_n(t_{j+1})\rangle| < 1-\varepsilon, \tag{37b}$$

where $0 < \varepsilon \ll 1$ is a small parameter. Condition (37b) is required to be valid for all adjacent points along all branches. If the criterion (37b) is violated, the sign swap decision is regarded as too uncertain and a new point $t^* = (t_j + t_{j+1})/2$ is introduced for improved tracking of the eigenvalue branches. The procedure is repeated until it stops after a finite number of iterations. For $\varepsilon = 10^{-2}$ the approach results in very well resolved sequences of eigenvalues and eigenfunctions that precisely track all features along the eigenvalue branches, in particular all avoided crossings. The basic grid obtained this way is further refined by interpolation for the dynamical simulations as described above in Sec. 3.4.

D Numerical Propagation Scheme

In this section, we describe the numerical propagation schemes to solve the TDSE (30) and the inhomogeneous TDSE (31) arising in the optimal control problem. The numerical schemes will be stated for the evolution in the co-rotating frame.

D.1 Forward Problem

The TDSE (30) is an initial value problem that must be propagated forward in time. For fixed control and initial conditions the solution is unique. In Sec. 3.3, the TDSE has been recast as a system of ODEs for

complex-valued amplitudes (25), which we state here as

$$i\dot{\mathbf{C}}\left(t\right)=K\left(t\right)\mathbf{C}\left(t\right). \tag{38}$$

Here we have introduced the generator of the evolution as $K\left(t\right)=\tilde{S}\left(t\right)+\sum_{k=1}^{6}u_{k}\left(t\right)\tilde{W}^{k}\left(t\right)$ in the co-rotating frame. The system operators and the control signals $u_{k}\left(t\right)$ are available at a discrete set of points in time. On the step from $\mathbf{C}\left(t\right)$ to $\mathbf{C}\left(t+\Delta t\right)$, we compute the matrix exponential

$$\mathbf{C}\left(t+\Delta t\right)\approx\mathrm{e}^{-i\overline{K}\Delta t}\,\mathbf{C}\left(t\right), \tag{39}$$

where $\overline{K}=\left(K\left(t\right)+K\left(t+\Delta t\right)\right)/2$ is the arithmetic mean of the K-operators on the limits of the considered time interval. As $\overline{K}$ is Hermitian, the scheme (39) preserves the norm exactly: $\left\|\mathbf{C}\left(t+\Delta t\right)\right\|^{2}=\left\|\mathbf{C}\left(t\right)\right\|^{2}$.

In order to avoid expensive computation of matrix exponentials, one can use the decomposition $\overline{K}\Delta t=Q\Sigma Q^{\dagger}$, where Σ is a diagonal matrix that contains the eigenvalues and $Q^{\dagger}=Q^{-1}$ is unitary. The propagation step then reads

$$\mathbf{C}\left(t+\Delta t\right)=Q\,\mathrm{e}^{-i\Sigma}\,Q^{\dagger}\,\mathbf{C}\left(t\right), \tag{40}$$

which is computationally cheaper. The scheme (40) was used throughout this work. For large systems (*i.e.*, more eigenstates) it is useful to employ a Padé approximation of the matrix exponential. The lowest order Padé approximation yields the Crank–Nicolson scheme

$$\begin{aligned}\mathbf{C}\left(t+\Delta t\right)=&\left(I+\frac{i}{2}\overline{K}\Delta t\right)^{-1}\left(I-\frac{i}{2}\overline{K}\Delta t\right)\mathbf{C}\left(t\right)\\&+O\left(\Delta t^{3}\right),\end{aligned} \tag{41}$$

which still preserves the norm exactly and is second-order correct in Δt.

D.2 Backward Problem

The co-state equation (31a) is an inhomogeneous TDSE that is propagated backwards in time. Following the steps described in Sec. 13, the problem can be written as

$$\begin{aligned}i\dot{\mathbf{\Lambda}}\left(t\right)=&K\left(t\right)\mathbf{\Lambda}\left(t\right)\\&-i\left[M\left(t\right)-2\left(\mathbf{C}^{\dagger}\left(t\right)M\left(t\right)\mathbf{C}\left(t\right)\right)\right]M\left(t\right)\mathbf{C}\left(t\right).\end{aligned} \tag{42}$$

Here, the expansion ansatz (13) was employed again for the co-state wave function

$$\chi\left(\mathbf{r},t\right)=\left\langle\mathbf{r}|\chi\left(t\right)\right\rangle=\sum_{n}\lambda_{n}\left(t\right)\psi_{n}\left(\mathbf{r},t\right).$$

The amplitudes were subsequently transformed into the co-rotating frame via $\mathbf{\Lambda}\left(t\right)=R^{\dagger}\left(t\right)\boldsymbol{\lambda}\left(t\right)$ using the rotation matrix (24). The inhomogeneous term in Eq. (42) involves the matrix

$$M\left(t\right)=\sqrt{\frac{\hbar}{E_{\mathrm{ref}}}}\left(D\left(t\right)+\sum_{k=1}^{6}u_{k}\left(t\right)\tilde{W}^{k}\left(t\right)\right),$$

that corresponds to the full Hamiltonian in the co-rotating frame. As before, we will consider the arithmetic mean $\overline{M}=\left(M\left(t\right)+M\left(t+\Delta t\right)\right)/2$ on the step from $t+\Delta t\rightarrow t$ in the numerical scheme for Eq. (42).

The homogeneous part of the problem is eliminated by the transformation $\mathbf{X}(s) = \mathrm{e}^{i\overline{K}(s-t)}\mathbf{\Lambda}(s)$, which leads to

$$\dot{\mathbf{X}}(s) = -\mathrm{e}^{i\overline{K}(s-t)}\left(\overline{M} - 2\left(\mathbf{C}^{\dagger}(s)\,\overline{M}\mathbf{C}(s)\right)\right)\overline{M}\mathbf{C}(s)$$

and $\mathbf{X}(t) = \mathbf{\Lambda}(t)$. Direct integration yields

$$\mathbf{X}(t+\Delta t) - \mathbf{X}(t) = -\int_t^{t+\Delta t} \mathrm{d}s\,\mathrm{e}^{i\overline{K}(s-t)}\left(\overline{M} - 2\left(\mathbf{C}^{\dagger}(s)\,\overline{M}\mathbf{C}(s)\right)\right)\overline{M}\mathbf{C}(s)$$

Using the scheme for the state-variable (39), we arrive at

$$\begin{aligned}\mathbf{X}(t+\Delta t) = \mathbf{X}(t) &- \int_0^{\Delta t} \mathrm{d}\tau\, Y_2(\tau)\,\mathbf{C}(t) \\ &+ 2\int_0^{\Delta t} \mathrm{d}\tau\,\left(\mathbf{C}^{\dagger}(t)\,Y_1(\tau)\,\mathbf{C}(t)\right) Y_1(\tau)\,\mathbf{C}(t)\end{aligned}$$

where $Y_n(\tau) = \mathrm{e}^{i\overline{K}\tau}\overline{M}^n\mathrm{e}^{-i\overline{K}\tau}$. In order to derive a scheme for (42) that is second-order in Δt, we expand $Y_n(\tau)$ to first order as $Y_n(\tau) = \overline{M}^n + i\left[\overline{K}, \overline{M}^n\right]\tau + O(\tau^2)$. Evaluation of the corresponding integrals and transformation back to $\mathbf{\Lambda}(t)$ yields the time-stepping scheme

$$\begin{aligned}\mathbf{\Lambda}(t) = \mathrm{e}^{+i\overline{K}\Delta t}&\mathbf{\Lambda}(t+\Delta t) \\ &+ \Delta t\left(\overline{M} - 2\left\langle\overline{M}\right\rangle_{\mathbf{C}(t)}\right)\overline{M}\mathbf{C}(t) \\ &+ i\frac{\Delta t^2}{2}\left(\left[\overline{K}, \overline{M}^2\right] - 2\left\langle\overline{M}\right\rangle_{\mathbf{C}(t)}\left[\overline{K}, \overline{M}\right] - 2\left\langle\left[\overline{K}, \overline{M}\right]\right\rangle_{\mathbf{C}(t)}\overline{M}\right)\mathbf{C}(t) \\ &+ O\left(\Delta t^3\right)\end{aligned} \tag{43}$$

where $\left\langle\overline{M}\right\rangle_{\mathbf{C}(t)} = \mathbf{C}^{\dagger}(t)\,\overline{M}\mathbf{C}(t)$.

In the absence of the inhomogeneous term, the scheme 43 reduces to a norm-preserving (unitary) integrator for the corresponding homogeneous TDSE.

References

[1] D. Loss and D. P. DiVincenzo, "Quantum computation with quantum dots", Phys. Rev. A **57**, 120–126 (1998) DOI: 10.1103/PhysRevA.57.120.

[2] F. A. Zwanenburg, A. S. Dzurak, A. Morello, M. Y. Simmons, L. C. L. Hollenberg, G. Klimeck, S. Rogge, S. N. Coppersmith, and M. A. Eriksson, "Silicon quantum electronics", Rev. Mod. Phys. **85**, 961–1019 (2013) DOI: 10.1103/RevModPhys.85.961.

[3] L. M. K. Vandersypen and M. A. Eriksson, "Quantum computing with semiconductor spins", Phys. Today **72**, 38–45 (2019) DOI: 10.1063/PT.3.4270.

[4] G. Burkard, T. D. Ladd, A. Pan, J. M. Nichol, and J. R. Petta, "Semiconductor spin qubits", Rev. Mod. Phys. **95**, 025003 (2023) DOI: 10.1103/RevModPhys.95.025003.

[5] A. M. Tyryshkin, S. Tojo, J. J. L. Morton, H. Riemann, N. V. Abrosimov, P. Becker, H.-J. Pohl, T. Schenkel, M. L. W. Thewalt, K. M. Itoh, and S. A. Lyon, "Electron spin coherence exceeding seconds in high-purity silicon", Nat. Mater. **11**, 143–147 (2011) DOI: 10.1038/nmat3182.

[6] A. Wild, J. Kierig, J. Sailer, J. W. Ager, E. E. Haller, G. Abstreiter, S. Ludwig, and D. Bougeard, "Few electron double quantum dot in an isotopically purified ^{28}Si quantum well", Appl. Phys. Lett. **100**, 143110 (2012) DOI: 10.1063/1.3701588.

[7] J. T. Muhonen, J. P. Dehollain, A. Laucht, F. E. Hudson, R. Kalra, T. Sekiguchi, K. M. Itoh, D. N. Jamieson, J. C. McCallum, A. S. Dzurak, and A. Morello, "Storing quantum information for 30 seconds in a nanoelectronic device", Nat. Nanotechnol. **9**, 986–991 (2014) DOI: 10.1038/NNANO.2014.211.

[8] J. Yoneda, K. Takeda, T. Otsuka, T. Nakajima, M. R. Delbecq, G. Allison, T. Honda, T. Kodera, S. Oda, Y. Hoshi, N. Usami, K. M. Itoh, and S. Tarucha, "A quantum-dot spin qubit with coherence limited by charge noise and fidelity higher than 99.9%", Nat. Nanotechnol. **13**, 102–106 (2018) DOI: 10.1038/s41565-017-0014-x.

[9] D. M. Zajac, A. J. Sigillito, M. Russ, F. Borjans, J. M. Taylor, G. Burkard, and J. R. Petta, "Resonantly driven CNOT gate for electron spins", Science **359**, 439–442 (2018) DOI: 10.1126/science.aao5965.

[10] L. Petit, H. G. J. Eenink, M. Russ, W. I. L. Lawrie, N. W. Hendrickx, S. G. J. Philips, J. S. Clarke, L. M. K. V, and M. Veldhorst, "Universal quantum logic in hot silicon qubits", Nature **580**, 355–359 (2020) DOI: 10.1038/s41586-020-2170-7.

[11] A. R. Mills, C. R. Guinn, M. J. Gullans, A. J. Sigillito, M. M. Feldman, E. Nielsen, and J. R. Petta, "Two-qubit silicon quantum processor with operation fidelity exceeding 99%", Sci. Adv. **8**, eabn5130 (2022) DOI: 10.1126/sciadv.abn5130.

[12] X. Xue, M. Russ, N. Samkharadze, B. Undseth, A. Sammak, G. Scappucci, and L. M. K. Vandersypen, "Quantum logic with spin qubits crossing the surface code threshold", Nature **601**, 343–347 (2022) DOI: 10.1038/s41586-021-04273-w.

[13] A. Noiri, K. Takeda, T. Nakajima, T. Kobayashi, A. Sammak, G. Scappucci, and S. Tarucha, "Fast universal quantum gate above the fault-tolerance threshold in silicon", Nature **601**, 338–342 (2022) DOI: 10.1038/s41586-021-04182-y.

[14] L. M. K. Vandersypen, H. Bluhm, J. S. Clarke, A. S. Dzurak, R. Ishihara, A. Morello, D. J. Reilly, L. R. Schreiber, and M. Veldhorst, "Interfacing spin qubits in quantum dots and donors—hot, dense, and coherent", npj Quantum Inf. **3**, 34 (2017) DOI: 10.1038/s41534-017-0038-y.

[15] M. Boerkamp, "Intel releases 12-qubit silicon quantum chip", Phys. World **36**, 11ii–11ii (2023) DOI: 10.1088/2058-7058/36/08/17.

[16] M. Veldhorst, H. G. J. Eenink, C. H. Yang, and A. S. Dzurak, "Silicon CMOS architecture for a spin-based quantum computer", Nat. Commun. **8**, 1766 (2017) DOI: 10.1038/s41467-017-01905-6.

[17] T. Fujita, T. A. Baart, C. Reichl, W. Wegscheider, and L. M. K. Vandersypen, "Coherent shuttle of electron-spin states", npj Quantum Inf. **3**, 22 (2017) DOI: 10.1038/s41534-017-0024-4.

[18] T. A. Baart, M. Shafiei, T. Fujita, C. Reichl, W. Wegscheider, and L. M. K. Vandersypen, "Single-spin CCD", Nat. Nanotechnol. **11**, 330–334 (2016) DOI: 10.1038/NNANO.2015.291.

[19] A. R. Mills, D. M. Zajac, M. J. Gullans, F. J. Schupp, T. M. Hazard, and J. R. Petta, "Shuttling a single charge across a one-dimensional array of silicon quantum dots", Nat. Commun. **10**, 1063 (2019) DOI: 10.1038/s41467-019-08970-z.

[20] J. Yoneda, W. Huang, M. Feng, C. H. Yang, K. W. Chan, T. Tanttu, W. Gilbert, R. C. C. Leon, F. E. Hudson, K. M. Itoh, A. Morello, S. D. Bartlett, A. Laucht, A. Saraiva, and A. S. Dzurak, "Coherent spin qubit transport in silicon", Nat. Commun. **12**, 4114 (2021) DOI: 10.1038/s41467-021-24371-7.

[21] V. Langrock, J. A. Krzywda, N. Focke, I. Seidler, L. R. Schreiber, and Ł. Cywiński, "Blueprint of a scalable spin qubit shuttle device for coherent mid-range qubit transfer in disordered Si/SiGe/SiO_2", PRX Quantum **4**, 020305 (2023) DOI: 10.1103/PRXQuantum.4.020305.

[22] A. M. J. Zwerver, S. V. Amitonov, S. L. de Snoo, M. T. Mądzik, M. Rimbach-Russ, A. Sammak, G. Scappucci, and L. M. K. Vandersypen, "Shuttling an electron spin through a silicon quantum dot array", PRX Quantum **4**, 030303 (2023) DOI: 10.1103/PRXQuantum.4.030303.

[23] F. van Riggelen-Doelman, C.-A. Wang, S. L. de Snoo, W. I. L. Lawriea, N. W. Hendrickx, M. Rimbach-Russ, A. Sammak, G. Scappucci, C. Déprez, and M. Veldhorst, "Coherent spin qubit shuttling through germanium quantum dots", DOI: 10.48550/arXiv.2308.02406 (2023) DOI: 10.48550/arXiv.2308.02406.

[24] I. Seidler, T. Struck, R. Xue, N. Focke, S. Trellenkamp, H. Bluhm, and L. R. Schreiber, "Conveyor-mode single-electron shuttling in Si/SiGe for a scalable quantum computing architecture", npj Quantum Inf. **8**, 100 (2022) DOI: 10.1038/s41534-022-00615-2.

[25] R. Xue, M. Beer, I. Seidler, S. Humpohl, J.-S. Tu, S. Trellenkamp, T. Struck, H. Bluhm, and L. R. Schreiber, "Si/SiGe qubus for single electron information-processing devices with memory and micron-scale connectivity function", DOI: 10.48550/arXiv.2306.16375 (2023) DOI: 10.48550/arXiv.2306.16375.

[26] T. Struck, M. Volmer, L. Visser, T. Offermann, R. Xue, J.-S. Tu, S. Trellenkamp, Ł. Cywiński, H. Bluhm, and L. R. Schreiber, "Spin-EPR-pair separation by conveyor-mode single electron shuttling in Si/SiGe", DOI: 10.48550/arXiv.2307.04897 (2023) DOI: 10.48550/arXiv.2307.04897.

[27] J. M. Taylor, H.-A. Engel, W. Dür, A. Yacoby, C. M. Marcus, P. Zoller, and M. D. Lukin, "Fault-tolerant architecture for quantum computation using electrically controlled semiconductor spins", Nat. Phys. **1**, 177–183 (2005) DOI: 10.1038/nphys174.

[28] M. Künne, A. Willmes, M. Oberländer, C. Gorjaew, J. D. Teske, H. Bhardwaj, M. Beer, E. Kammerloher, R. Otten, I. Seidler, R. Xue, L. R. Schreiber, and H. Bluhm, "The SpinBus architecture: scaling spin qubits with electron shuttling", DOI: 10.48550/arXiv.2306.16348 (2023) DOI: 10.48550/arXiv.2306.16348.

[29] J. M. Boter, J. P. Dehollain, J. P. van Dijk, Y. Xu, T. Hensgens, R. Versluis, H. W. Naus, J. S. Clarke, M. Veldhorst, F. Sebastiano, and L. M. Vandersypen, "Spiderweb array: a sparse spin-qubit array", Phys. Rev. Appl. **18**, 024053 (2022) DOI: 10.1103/PhysRevApplied.18.024053.

[30] N. P. de Leon, K. M. Itoh, D. Kim, K. K. Mehta, T. E. Northup, H. Paik, B. S. Palmer, N. Samarth, S. Sangtawesin, and D. W. Steuerman, "Materials challenges and opportunities for quantum computing hardware", Science **372**, eabb2823 (2021) DOI: 10.1126/science.abb2823.

[31] T. Struck, A. Hollmann, F. Schauer, O. Fedorets, A. Schmidbauer, K. Sawano, H. Riemann, N. V. Abrosimov, Ł. Cywiński, D. Bougeard, and L. R. Schreiber, "Low-frequency spin qubit energy splitting noise in highly purified ^{28}Si/SiGe", npj Quantum Information **6**, 2056–6387 (2020) DOI: 10.1038/s41534-020-0276-2.

[32] D. D. Esposti, L. E. A. Stehouwer, Önder Gül, N. Samkharadze, C. Déprez, M. Meyer, I. N. Meijer, L. Tryputen, S. Karwal, M. Botifoll, J. Arbiol, S. V. Amitonov, L. M. K. Vandersypen, A. Sammak, M. Veldhorst, and G. Scappucci, *Low disorder and high valley splitting in silicon*, 2023, DOI: 10.48550/arXiv.2309.02832.

[33] B. Paquelet Wuetz, M. P. Losert, S. Koelling, L. E. A. Stehouwer, A.-M. J. Zwerver, S. G. J. Philips, M. T. Mądzik, X. Xue, G. Zheng, M. Lodari, S. V. Amitonov, N. Samkharadze, A. Sammak, L. M. K. Vandersypen, R. Rahman, S. N. Coppersmith, O. Moutanabbir, M. Friesen, and G. Scappucci, "Atomic fluctuations lifting the energy degeneracy in Si/SiGe quantum dots", Nat. Commun. **13**, 7730 (2022) DOI: 10.1038/s41467-022-35458-0.

[34] P. G. Evans, D. E. Savage, J. R. Prance, C. B. Simmons, M. G. Lagally, S. N. Coppersmith, M. A. Eriksson, and T. U. Schülli, "Nanoscale distortions of Si quantum wells in Si/SiGe quantum-electronic heterostructures", Advanced Materials **24**, 5217–5221 (2012) DOI: 10.1002/adma.201201833.

[35] I. Seidler, M. Neul, E. Kammerloher, M. Künne, A. Schmidbauer, L. K. Diebel, A. Ludwig, J. Ritzmann, A. D. Wieck, D. Bougeard, H. Bluhm, and L. R. Schreiber, "Tailoring potentials by simulation-aided design of gate layouts for spin-qubit applications", Phys. Rev. Appl. **20**, 044058 (2023) DOI: 10.1103/PhysRevApplied.20.044058.

[36] C. Corley-Wiciak, M. Zoellner, I. Zaitsev, K. Anand, E. Zatterin, Y. Yamamoto, A. Corley-Wiciak, F. Reichmann, W. Langheinrich, L. R. Schreiber, C. Manganelli, M. Virgilio, C. Richter, and G. Capellini, "Lattice deformation at submicron scale: X-ray nanobeam measurements of elastic strain in electron shuttling devices", Phys. Rev. Appl. **20**, 024056 (2023) DOI: 10.1103/PhysRevApplied.20.024056.

[37] O. V. Ivakhnenko, S. N. Shevchenko, and F. Nori, "Nonadiabatic Landau–Zener–Stückelberg–Majorana transitions, dynamics, and interference", Phys. Rep. **995**, 1–89 (2023) DOI: 10.1016/j.physrep.2022.10.002.

[38] H. Si, "Tetgen, a delaunay-based quality tetrahedral mesh generator", ACM Trans. Math. Software **41**, 1–36 (2015) DOI: 10.1145/2629697.

[39] J. Fuhrmann, *VoronoiFVM.jl – Finite volume solver for coupled nonlinear partial differential equations*, online, https://github.com/j-fu/VoronoiFVM.jl, 2023, DOI: 10.5281/zenodo.3529808.

[40] B. Schmidt and U. Lorenz, "WavePacket: a Matlab package for numerical quantum dynamics. I: Closed quantum systems and discrete variable representations", Comput. Phys. Commun. **213**, 223–234 (2017) DOI: 10.1016/j.cpc.2016.12.007.

[41] J. J. Sakurai and J. Napolitano, *Modern quantum mechanics*, 2nd ed. (Cambridge University Press, Cambridge, 2017), DOI: 10.1017/9781108499996.

[42] I. N. Levine, *Quantum chemistry*, 7th ed. (Pearson, Boston, 2014).

[43] R. B. Lehoucq, D. C. Sorensen, and C. Yang, *ARPACK users' guide: solution of large-scale eigenvalue problems with implicitly restarted Arnoldi methods* (Society for Industrial and Applied Mathematics (SIAM), Philadelphia, 1998).

[44] L. N. Trefethen, *Spectral methods in MATLAB* (Society for Industrial and Applied Mathematics (SIAM), Philadelphia, 2000), DOI: 10.1137/1.9780898719598.

[45] E. P. Glasbrenner and W. P. Schleich, "The Landau–Zener formula made simple", J. Phys. B: At., Mol. Opt. Phys. **56**, 104001 (2023) DOI: 10.1088/1361-6455/acc774.

[46] B. Venitucci, L. Bourdet, D. Pouzada, and Y.-M. Niquet, "Electrical manipulation of semiconductor spin qubits within the g-matrix formalism", Phys. Rev. B **98**, 155319 (2018) DOI: 10.1103/PhysRevB.98.155319.

[47] A. Crippa, R. Maurand, L. Bourdet, D. Kotekar-Patil, A. Amisse, X. Jehl, M. Sanquer, R. Laviéville, H. Bohuslavskyi, L. Hutin, S. Barraud, M. Vinet, Y.-M. Niquet, and S. De Franceschi, "Electrical spin driving by g-matrix modulation in spin-orbit qubits", Phys. Rev. Lett. **120**, 137702 (2018) DOI: 10.1103/PhysRevLett.120.137702.

[48] V. N. Golovach, A. Khaetskii, and D. Loss, "Phonon-induced decay of the electron spin in quantum dots", Phys. Rev. Lett. **93**, 016601 (2004) DOI: 10.1103/PhysRevLett.93.016601.

[49] C. Tahan and R. Joynt, "Relaxation of excited spin, orbital, and valley qubit states in ideal silicon quantum dots", Phys. Rev. B **89**, 075302 (2014) DOI: 10.1103/PhysRevB.89.075302.

[50] M. V. Berry, “Transitionless quantum driving”, Journal of Physics A: Mathematical and Theoretical **42**, 365303 (2009) DOI: 10.1088/1751-8113/42/36/365303.

[51] J Werschnik and E. K. U. Gross, “Quantum optimal control theory”, J. Phys. B: At., Mol. Opt. Phys. **40**, R175–R211 (2007) DOI: 10.1088/0953-4075/40/18/R01.

[52] U. Boscain, M. Sigalotti, and D. Sugny, “Introduction to the Pontryagin maximum principle for quantum optimal control”, PRX Quantum **2**, 030203 (2021) DOI: 10.1103/PRXQuantum.2.030203.

[53] J. Nocedal and S. J. Wright, *Numerical optimization*, 2nd ed., Springer Series in Operations Research and Financial Engineering (Springer, New York, 2006), DOI: 10.1007/978-0-387-40065-5.

[54] N. Khaneja, T. Reiss, C. Kehlet, T. Schulte-Herbrüggen, and S. J. Glaser, “Optimal control of coupled spin dynamics: design of NMR pulse sequences by gradient ascent algorithms”, J. Magn. Reson. **172**, 296–305 (2005) DOI: 10.1016/j.jmr.2004.11.004.

[55] P. de Fouquieres, S. Schirmer, S. Glaser, and I. Kuprov, “Second order gradient ascent pulse engineering”, J. Magn. Reson. **212**, 412–417 (2011) DOI: 10.1016/j.jmr.2011.07.023.

[56] J. Barzilai and J. M. Borwein, “Two-point step size gradient methods”, IMA J. Numer. Anal. **8**, 141–148 (1988) DOI: 10.1093/imanum/8.1.141.

[57] G von Winckel and A Borzì, “Computational techniques for a quantum control problem with H^1-cost”, Inverse Prob. **24**, 034007 (2008) DOI: 10.1088/0266-5611/24/3/034007.

[58] T. McJunkin, B. Harpt, Y. Feng, M. P. Losert, R. Rahman, J. P. Dodson, M. A. Wolfe, D. E. Savage, M. G. Lagally, S. N. Coppersmith, M. Friesen, R. Joynt, and M. A. Eriksson, “SiGe quantum wells with oscillating Ge concentrations for quantum dot qubits”, Nat. Commun. **13**, 7777 (2022) DOI: 10.1038/s41467-022-35510-z.

[59] M. P. Losert, M. A. Eriksson, R. Joynt, R. Rahman, G. Scappucci, S. N. Coppersmith, and M. Friesen, “Practical strategies for enhancing the valley splitting in Si/SiGe quantum wells”, Phys. Rev. B **108**, 125405 (2023) DOI: 10.1103/PhysRevB.108.125405.

[60] B. D. Woods, H. Soomro, E. S. Joseph, C. C. D. Frink, R. Joynt, M. A. Eriksson, and M. Friesen, “Coupling conduction-band valleys in modulated SiGe heterostructures via shear strain”, DOI: 10.48550/arXiv.2310.18879 (2023) DOI: 10.48550/arXiv.2310.18879.

[61] G. Scappucci, C. Kloeffel, F. A. Zwanenburg, D. Loss, M. Myronov, J.-J. Zhang, S. D. Franceschi, G. Katsaros, and M. Veldhorst, “The germanium quantum information route”, Nature Reviews Materials **6**, 926–943 (2021) DOI: 10.1038/s41578-020-00262-z.

[62] F. Schäffler, “High-mobility si and ge structures”, Semicond. Sci. Technol. **12**, 1515–1549 (1997) DOI: 10.1088/0268-1242/12/12/001.